

# Unrolling Plug-and-Play Gradient Graph Laplacian Regularizer for Image Restoration

Jianghe Cai, Gene Cheung, *Fellow, IEEE*, Fei Chen, *Member, IEEE*

**Abstract**—Generic deep learning (DL) networks for image restoration like denoising and interpolation lack mathematical interpretability, require voluminous training data to tune a large parameter set, and are fragile in the face of covariate shift. To address these shortcomings, we build interpretable networks by unrolling variants of a graph-based optimization algorithm of different complexities. Specifically, for a general linear image formation model, we first formulate a convex quadratic programming (QP) problem with a new  $\ell_2$ -norm graph smoothness prior called gradient graph Laplacian regularizer (GGLR) that promotes piecewise planar (PWP) signal reconstruction. To solve the posed unconstrained QP problem, instead of computing a linear system solution straightforwardly, we introduce a variable number of auxiliary variables and correspondingly design a family of ADMM algorithms. We then unroll them into variable-complexity feed-forward networks, amenable to parameter tuning via back-propagation. More complex unrolled networks require more labeled data to train more parameters, but have better overall performance. The unrolled networks have periodic insertions of a graph learning module, akin to a self-attention mechanism in a transformer architecture, to learn pairwise similarity structure inherent in data. Experimental results show that our unrolled networks perform competitively to generic DL networks in image restoration quality while using only a fraction of parameters, and demonstrate improved robustness to covariate shift.

**Index Terms**—Image restoration, Graph signal processing, Plug-and-Play ADMM, Algorithm unrolling.

## I. INTRODUCTION

**I**MAGE restoration, such as denoising and interpolation, aims to recover the original image given only a noise-corrupted / sub-sampled / filtered observation. Existing image restoration methods can be broadly categorized into *model-based* and *data-driven* approaches. To regularize an ill-posed signal restoration problem, model-based methods adopt mathematically defined signal priors such as sparse representation [1], *total variation* (TV) [2], and low-rank matrices [3]. However, while these assumed priors are easily interpretable, they tend to be overly restrictive in assumptions, resulting in sub-par performance in practical scenarios.

In contrast, advances in *deep learning* (DL) have led to *deep neural nets* (DNN) that achieve state-of-the-art (SOTA) performance after intensive training on large datasets [4], [5].

The work of G. Cheung was supported in part by the Natural Sciences and Engineering Research Council of Canada (NSERC) RGPIN-2019-06271, RGPAS-2019-00110. The work of F. Chen was supported in part by the National Natural Science Foundation of China (62471141). (*Corresponding author: Fei Chen*)

J. Cai and F. Chen are with College of Computer and Data Science, Fuzhou University, Fuzhou, China (e-mail:chenfei314@fzu.edu.cn).

G. Cheung is with the department of EECS, York University, 4700 Keele Street, Toronto, M3J 1P3, Canada (e-mail: genec@yorku.ca).

However, generic DNNs have known drawbacks. First, generic DNN architectures operate like “black boxes” that are difficult to interpret. Second, generic DNNs require tuning of large parameter sets from huge training data, which may be impractical for scenarios where it is difficult or expensive to obtain large labeled datasets. Training millions of parameters on energy-hungry server farms is also environmentally unfriendly. Third, in the event of *covariate shift*—where statistics of training and testing data differ [6], [7]—performance of trained DNNs can degrade precipitously.

Instead of generic off-the-shelf DNNs, *algorithm unrolling*—implementing iterations of an iterative optimization algorithm as neural layers for end-to-end parameter tuning—offers an alternative approach to build problem-specific networks [8]. Unrolled networks can be competitive in performance; specifically, [9] recently showed that multi-head self-attention operator and multi-layer perceptron in transformer can be interpreted as gradient descent and sparsifying operators that alternately minimize a sparse rate reduction (SRR) objective. While the unrolled network in [9]—called a “white-box” transformer—is 100% mathematically interpretable and on-par with SOTA transformers in a range of vision tasks, tuning of the resulting large parameter set is still formidable.

Inspired by [9], in this paper, leveraging recent progress in *graph signal processing* (GSP) [10], [11] to solve signal restoration problems [12]–[19], we build neural networks by unrolling variants of a graph-based optimization algorithm of different complexities. Like [9], our unrolled networks are mathematically interpretable, but because our parameter set of variable size is dramatically smaller, the required training dataset is also small, resulting in networks that are more robust to covariate shift.

Specifically, given a general linear image formation model, we first formulate a convex *quadratic programming* (QP) optimization problem using a recent  $\ell_2$ -norm graph smoothness prior *gradient graph Laplacian regularizer* (GGLR) [20] that promotes *piecewise planar* (PWP) signal reconstruction. To solve the posed unconstrained QP problem, instead of computing a linear system solution straightforwardly using a known solver such as *conjugate gradient* (CG) [21], we introduce a varying number of auxiliary variables corresponding to sums of GGLRs on pixel rows and columns of a target patch. To address the modified multi-variable QP optimization, we design a family of *alternating direction method of multipliers* (ADMM) algorithms [22] and unroll them into feed-forward networks—amenable to parameter optimization via back-propagation. We call our networks *unrolled Plug-and-Play GGLR* (UPnPGGLR). More complex UPnP GGLRs contain more parameters

that required training on larger datasets, but often lead to better overall performance.

Crucially, our UPnPGLRs have periodic insertions of a graph learning module that learns pairwise similarity structure inherent in data. We show that this module is akin to a self-attention mechanism [23] in a conventional transformer architecture [24], but doing so in a much more parameter-efficient manner, thanks to a shallow *convolutional neural net* (CNN) implementation that maps input embeddings to low-dimensional feature vectors for edge weight computation. This results in a lightweight transformer-like neural net that is also mathematically interpretable<sup>1</sup>, similar in philosophy<sup>2</sup> to [9].

Experimental results for a range of image restoration tasks—denoising, interpolation and non-blind deblurring—show that our UPnPGLRs perform competitively to SOTA generic DL networks, while using only a tiny fraction of parameters (*e.g.*, fewer than 1% of parameters in Restormer [25] for denoising), and demonstrate improved robustness to covariate shift. In summary, our main contributions are

- 1) For graph learning, we adopt shallow CNNs to learn low-dimensional features for edge weight computation. This amounts to a parameter-efficient variant of the self-attention mechanism typical in a transformer architecture.
- 2) Starting from a linear image formation model, we formulate a restoration problem using  $\ell_2$ -norm GGLR as prior, resulting in an unconstrained QP optimization problem.
- 3) We introduce a varying number of auxiliary variables covering different GGLR subset sums, leading to a family of ADMM algorithms of different complexities.
- 4) We unroll our family of algorithms into feed-forward networks (UPnPGLRs) for tuning of a variable number of parameters via back-propagation. In image restoration scenarios such as denoising, interpolation and non-blind deblurring, we show that our interpretable UPnPGLRs achieve SOTA restoration quality while employing significantly fewer parameters. We demonstrate also improved robustness to covariate shift.

The rest of the paper is organized as follows. We first overview related works in Section II. We review essential graph definitions and graph smoothness priors in Section III. We formulate the image restoration problem using GGLR as prior, and describe our family of corresponding ADMM-based optimization algorithms of variable complexities in Section IV. We describe our unrolled network architecture, including periodic insertions of the important graph learning module in Section V. Finally, experiments and conclusion are presented in Section VI and VII, respectively.

<sup>1</sup>Common in algorithm unrolling [8], “interpretable” here means that each unrolled neural layer corresponds to a specific iteration of a model-based iterative optimization algorithm. In our work, we construct a graph learning module for graph-based optimization, where the edge weight learning and normalization components can be interpreted respectively as attention weight learning and the softmax operation in a self-attention mechanism.

<sup>2</sup>While [9] designed an optimization algorithm minimizing a sparse rate reduction (SRR) objective, we design a low-pass filter minimizing GGLR, interleaving with a graph learning module. In our case, each graph learning module corresponds to attention weight learning, while the GGLR-based optimization corresponds to attention-based filtering.

**Notation:** Vectors and matrices are written in bold lowercase and uppercase letters, respectively. The  $(i, j)$  element and the  $j$ -th column of a matrix  $\mathbf{A}$  are denoted by  $A_{i,j}$  and  $\mathbf{a}_j$ , respectively. The  $i$ -th element in the vector  $\mathbf{v}$  is denoted by  $v_i$ . The square identity matrix of rank  $N$  is denoted by  $\mathbf{I}_N$ , the  $M$ -by- $N$  zero matrix is denoted by  $\mathbf{0}_{M,N}$ , and the vector of all ones / zeros of length  $N$  is denoted by  $\mathbf{1}_N / \mathbf{0}_N$ , respectively.

## II. RELATED WORKS

### A. Learning-based Image Restoration

Powerful generic DL networks are prevalent in image restoration. For example, DnCNN [26] utilizes residual learning and batch normalization to construct a DL network architecture, resulting in SOTA image denoising performance. By taking a tunable noise level map as input, FFDNet [27] can handle more complex noise scenarios. CBDNet [28] employs a noise estimation sub-net and integrates it into the network to accomplish blind restoration. To build a CNN capable of handling several noise levels, Vemulapalli *et al.* [29] employ conditional random field for regularization. Recently, transformer-based models have achieved superior results in image restoration [25], [30]–[32]. However, these models have substantially larger network sizes and require tuning of an ever-growing number of parameters to achieve such high performance. Moreover, they are not easy to generalize and suffer steep performance degradation when faced with mismatched statistics between training and test data [33], [34]. In contrast, our UPnPGLRs achieve comparable denoising performance while employing dramatically fewer parameters and are more robust to covariate shift.

### B. Model-based Image Restoration

Defining signal priors using mathematical models was widespread in early image restoration literature; popular model-based denoisers include bilateral filter [35], non-local means (NLM) [36], and BM3D [37]. More recent model-based methods including trilateral weighted sparse coding (TWSC) [38] and non-local self-similarity (NSS) [39]. While these methods are interpretable and robust to covariate shift, we will demonstrate in Section VI that their denoising performances are noticeably sub-par compared to SOTA DNNs, due to their overly restrictive assumed models. In contrast, *our UPnPGLRs achieve competitive performance while enabling interpretability and covariate shift robustness, thanks to our flexible graph model that is parameterized by low-dimensional features learned from data*.

Recently, graph smoothness priors from the GSP field [10], [11]—study of discrete signals on irregular data kernels described by graphs—have been successfully applied to image restoration problems such as denoising [12], dequantization [13], and deblurring [15]. In particular, *graph Laplacian regularizer* (GLR) [12] is popular, due to its effective promotion of *piecewise constant* (PWC) signal reconstruction and its convenient quadratic form. In this paper, we employ instead its generalization GGLR [20] defined on gradient graphs that promotes PWP signal reconstruction.

Note that GGLR was studied only from a model-based perspective in [20], where the minimization of the  $\ell_2$ -norm objective is solved by computing a system of linear equations directly using CG. In contrast, in this paper we demonstrate how GGLR can be practically implemented in combination with recent deep learning technologies; in particular, for image restoration we first introduce a varying number of auxiliary variables to the  $\ell_2$ -norm objective, then design a family of ADMM algorithms that unroll into feed-forward networks of different complexities for data-driven parameter learning. Moreover, we show how pairwise similarity structures can be learned from data—akin to the self-attention mechanism in transformers—in order to specify the underlying graphs and the GGLR prior. We show in Section VI that our unrolled networks significantly outperform solving the linear system directly as done in [20].

Unrolling of GLR for image denoising was proposed in [40], and unrolling of *graph total variation* (GTV) was done in [41]. Unlike [40], we unroll GGLR instead using a varying number of auxiliary variables, resulting in a family of PnP-GGLR algorithms [22] and corresponding variable-complexity feed-forward networks with different numbers of tunable parameters. We show in Section VI that unrolling of GGLR outperforms unrolling of GLR and GTV in our experiments.

#### C. Plug-and-Play Methods for Image Restoration

Beyond the early PnP-ADMM work [22], there has been a plethora of PnP methods for image restoration; recent ones include [42]–[45]. [42] enforced equivariance to certain transformations, such as rotations and reflections, on the denoiser, resulting in improvement in stability and reconstruction of the restoration algorithm. [43], based on stochastic regularization, applied the denoiser only on images with noise of the adequate level, leading to a stochastic gradient descent algorithm that solves the ill-posed inverse problem. [44] extended the PnP idea by studying families of PnP iterations, where each iteration has an accompanied denoiser. [45] proposed an optimization framework based on proximal gradient, where the gradient update ensures the iterates remain in the solution-space, and an off-the-shelf denoiser can replace the proximal operator.

What is common among these PnP methods is that an implicit pre-trained denoiser is used as a basic building block in a larger optimization framework. In contrast, we employ a new GGLR regularization leading to a family of ADMM algorithms, that unroll into feed-forward networks for data-driven parameter tuning. That means unlike [42]–[45], our “denoiser” is specific and interpretable. Further, none of [42]–[45] explicitly contain a graph learning module that constitutes a self-attention mechanism—a key contribution in our work. Nonetheless, to demonstrate the superiority of our method, we compared UPnP-GGLR against [42] and [43] on image restoration tasks in our experiments.

#### D. Deep Algorithm Unrolling

The seminal work in algorithm unrolling [8] is the unrolling of *iterative soft-thresholding algorithm* (ISTA) in sparse coding into *Learned ISTA* (LISTA) [46]. Since then, algorithm

unrolling has been employed in a wide variety of algorithms for different applications, such as non-negative matrix factorization for speech processing [47], proximal gradient descent for medical imaging [48]. Instead of unrolling a *fixed* iterative algorithm, in this paper we vary the number of auxiliary variables to induce a family of PnP-GGLR algorithms, resulting in variable-complexity feed-forward networks for parameter tuning.

We note that the original PnP-ADMM [22] and many subsequent PnP works [42]–[45] assume an implicit pre-trained denoiser for solving a denoising sub-problem in an overall optimization framework. In contrast, our proposed family of algorithms focuses exclusively on GGLR as the chosen signal prior for image restoration. Nonetheless, we liberally abuse the terminology “PnP” here to mean that our setup permits the flexible use of any linear image formation model (accommodating applications such as denoising, interpolation and non-blind deblurring) and the introduction of a varying number of auxiliary variables, leading to unrolled networks of variable complexity.

### III. PRELIMINARIES

#### A. GSP Definitions

A graph  $\mathcal{G}(\mathcal{N}, \mathcal{E}, \mathbf{W})$  is defined by a node set  $\mathcal{N} = \{1, \dots, N\}$  and an edge set  $\mathcal{E}$ , where  $(i, j) \in \mathcal{E}$  means nodes  $i, j \in \mathcal{N}$  are connected with weight  $w_{i,j} = W_{i,j} \in \mathbb{R}$ . Fig. 1(a) shows an example of a 3-node line graph. We assume edges are undirected, and thus *adjacency matrix*  $\mathbf{W} \in \mathbb{R}^{N \times N}$  is symmetric. The *combinatorial graph Laplacian matrix* is defined as  $\mathbf{L} \triangleq \text{diag}(\mathbf{W}\mathbf{1}_N) - \mathbf{W} \in \mathbb{R}^{N \times N}$ , where  $\text{diag}(\mathbf{v})$  returns a diagonal matrix with  $\mathbf{v}$  along its diagonal. Real and symmetric  $\mathbf{L}$  is *positive semi-definite* (PSD) if  $w_{i,j} \geq 0, \forall i, j$ , i.e.,  $\mathbf{x}^\top \mathbf{L} \mathbf{x} \geq 0, \forall \mathbf{x}$  [11].

Real and symmetric  $\mathbf{L}$  can be eigen-decomposed to  $\mathbf{L} = \mathbf{V}\Sigma\mathbf{V}^\top$ , where  $\mathbf{V}$  contains eigenvectors of  $\mathbf{L}$  as columns, and  $\Sigma = \text{diag}(\lambda_1, \dots, \lambda_N)$  is a diagonal matrix with real and non-negative eigenvalues  $0 = \lambda_1 \leq \lambda_2 \leq \dots \leq \lambda_N$  along its diagonal. Eigen-pair  $(\lambda_k, \mathbf{v}_k)$  are the  $k$ -th graph frequency and Fourier mode for  $\mathcal{G}$ , respectively.  $\tilde{\mathbf{x}} = \mathbf{V}^\top \mathbf{x}$  is the *graph Fourier transform* (GFT) of signal  $\mathbf{x} \in \mathbb{R}^N$  [10].

#### B. Graph Laplacian Regularizer

To regularize an ill-posed graph signal restoration problem, the *graph Laplacian regularizer* (GLR) is often used due to its convenient quadratic form [12]. GLR for a signal  $\mathbf{x} \in \mathbb{R}^N$  is

$$\mathbf{x}^\top \mathbf{L} \mathbf{x} = \sum_{(i,j) \in \mathcal{E}} w_{i,j} (x_i - x_j)^2 = \sum_k \lambda_k \tilde{x}_k^2 \quad (1)$$

where  $\tilde{x}_k = \mathbf{v}_k^\top \mathbf{x}$  is the  $k$ -th graph frequency coefficient for signal  $\mathbf{x}$ . Thus, a *low-pass* signal with energies  $\tilde{x}_k$ ’s concentrated in low graph frequencies  $\lambda_k$ ’s would induce a small GLR value in (1).

Edge weights  $w_{i,j}$  can be defined in a *signal-dependent* manner, specifically,

$$w_{i,j}(x_i, x_j) = \exp \left( -\frac{\|\mathbf{f}_i - \mathbf{f}_j\|_2^2}{\sigma_f^2} - \frac{|x_i - x_j|^2}{\sigma_x^2} \right), \quad (2)$$

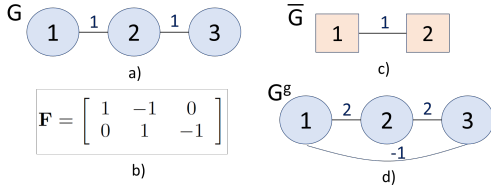


Fig. 1. A 3-node line graph  $G$  in (a), a gradient operator  $F \in \mathbb{R}^{2 \times 3}$  for a row or column of 3 pixels in (b), gradient graph  $\bar{G}$  in (c), and resulting GNG  $G^g$  in (d)—a signed graph with both positive and negative edges [18].

where  $\mathbf{f}_i \in \mathbb{R}^K$  is a *feature vector* for node  $i$ , and  $\sigma_f$  and  $\sigma_a$  are parameters. (2) is signal-dependent because of its dependency on signal samples  $x_i$  and  $x_j$ . Using edge weight definition (2) means GLR is also signal-dependent. Iteratively applying signal-dependent GLR promotes *piecewise constant* (PWC) signal reconstruction; see Appendix A for a detailed discussion.

### C. Gradient Graph Laplacian Regularizer

GGLR [20] applies GLR to the gradient of signal  $\mathbf{x}$  instead of  $\mathbf{x}$  directly; for 1D signals, a (piecewise) constant signal gradient means a (*piecewise*) *linear* (PWL) signal. For images, GGLR can mean applying GLR to horizontal/vertical image gradients separately. To compute horizontal/vertical gradient  $\boldsymbol{\alpha} \in \mathbb{R}^{N-1}$  for a pixel row/column  $\mathbf{x} \in \mathbb{R}^N$ , we first define a *gradient operator*  $\mathbf{F} \in \mathbb{R}^{N-1 \times N}$ :

$$F_{i,j} = \begin{cases} 1 & \text{if } i = j \\ -1 & \text{if } i = j - 1 \\ 0 & \text{o.w.} \end{cases}. \quad (3)$$

Note that  $\mathbf{F}\mathbf{1} = \mathbf{0}$  and  $\mathbf{F}$  is full row-rank [20]. We then compute horizontal/vertical gradients  $\boldsymbol{\alpha} \in \mathbb{R}^{N-1}$  as

$$\boldsymbol{\alpha} = \mathbf{F}\mathbf{x}. \quad (4)$$

A positive *gradient graph*  $\bar{G}$  is constructed to connect gradients  $i$  and  $j$  with non-negative weight  $\bar{w}_{i,j}$ , computed in a *gradient-dependent* manner, similarly to (2), as

$$\bar{w}_{i,j}(\alpha_i, \alpha_j) = \exp\left(-\frac{\|\mathbf{f}_i - \mathbf{f}_j\|_2^2}{\sigma_f^2} - \frac{|\alpha_i - \alpha_j|^2}{\sigma_a^2}\right), \quad (5)$$

where  $\mathbf{f}_i \in \mathbb{R}^K$  is a feature vector for gradient  $i$ , and  $\sigma_f$  and  $\sigma_a$  are learnable parameters. See Fig. 1(b) and (c) for an example of gradient operator  $\mathbf{F}$  for a 3-pixel row and the corresponding gradient graph  $\bar{G}$  for  $\boldsymbol{\alpha} \in \mathbb{R}^2$ , respectively.

Define a *gradient adjacency matrix*  $\bar{\mathbf{W}} \in \mathbb{R}^{(N-1) \times (N-1)}$  using the set of edge weights  $\{\bar{w}_{i,j}\}$ . Correspondingly, define *gradient graph Laplacian* matrix as  $\bar{\mathbf{L}} \triangleq \text{diag}(\bar{\mathbf{W}}\mathbf{1}_N) - \bar{\mathbf{W}}$ . Finally, GGLR is defined as

$$\mathbf{x}^\top \bar{\mathbf{L}} \boldsymbol{\alpha} = \mathbf{x}^\top \underbrace{\mathbf{F}^\top \bar{\mathbf{L}} \mathbf{F}}_{\mathcal{L}} \mathbf{x} = \mathbf{x}^\top \mathcal{L} \mathbf{x} \quad (6)$$

where  $\mathcal{L}$  is a *gradient-induced nodal graph* (GNG) Laplacian for a GNG  $G^g$ . [20] proved that the eigen-subspace corresponding to first eigenvalue  $\lambda_1 = 0$  of  $\mathcal{L}$  has dimension 2 (*i.e.*, multiplicity of eigenvalue  $\lambda_1$  is two), and spans the space of all linear signals  $\mathbf{x} = m\mathbf{i} + \mathbf{c}$ , where  $\mathbf{i}$  is the node index of line graph  $G$ , and  $m$  and  $\mathbf{c}$  are the respective slope and  $y$ -intercept

of the line. Thus, using GGLR  $\mathbf{x}^\top \mathcal{L} \mathbf{x}$  as signal prior “promotes” linear signal reconstruction (*i.e.*,  $\mathbf{x}^\top \mathcal{L} \mathbf{x} = 0$  for any linear  $\mathbf{x}$ ), and by extension signal-dependent GGLR promotes piecewise linear signal reconstruction. See Appendix B for a detailed discussion.

Fig. 1(d) shows an example of a GNG  $G^g$  corresponding to the gradient graph  $\bar{G}$  in (c). Note that in general,  $G^g$  is a *signed* graph with both positive and negative edges; a signed graph is necessary so that GGLR  $\mathbf{x}^\top \mathcal{L} \mathbf{x} = 0$  for any linear signal  $\mathbf{x}$ , as earlier discussed. However, given  $\bar{\mathbf{L}}$  is PSD,  $\mathcal{L} = \mathbf{F}^\top \bar{\mathbf{L}} \mathbf{F}$  must also be PSD, though  $G^g$  is a signed graph.

## IV. IMAGE RESTORATION VIA PLUG-AND-PLAY GGLR

### A. GGLR for Image Patches

1) *Horizontal/Vertical Line Graphs for Horizontal/Vertical Gradients*: Assuming a target patch is PWP, its pixel rows and columns must be PWL. Thus, to restore an  $N$ -by- $N$  image patch, we first employ GGLR as a prior for  $N$  individual pixel rows and  $N$  columns in the patch. Denote by  $\mathbf{x} \in \mathbb{R}^{N^2}$  the vectorized version of the patch by scanning pixels row-by-row. Denote by  $\mathbf{H}_k, \mathbf{G}_k \in \{0, 1\}^{N \times N^2}$  the respective sampling matrix that picks out  $N$  pixels of the  $k$ -th row/column from  $N^2$  entries in  $\mathbf{x}$ , *i.e.*,

$$H_{k,i,j} = \begin{cases} 1 & \text{if entry } j \text{ is the } i\text{-th pixel in } k\text{-th row} \\ 0 & \text{o.w.} \end{cases} \quad (7)$$

$$G_{k,i,j} = \begin{cases} 1 & \text{if entry } j \text{ is the } i\text{-th pixel in } k\text{-th column} \\ 0 & \text{o.w.} \end{cases} \quad (8)$$

For example,  $\mathbf{H}_1$  and  $\mathbf{G}_2$  that pick out the first row and the second column of a  $2 \times 2$  pixel patch are

$$\mathbf{H}_1 = \begin{bmatrix} 1 & 0 & 0 & 0 \\ 0 & 1 & 0 & 0 \end{bmatrix}, \quad \mathbf{G}_2 = \begin{bmatrix} 0 & 1 & 0 & 0 \\ 0 & 0 & 0 & 1 \end{bmatrix}. \quad (9)$$

For each  $k$ -th row/column of  $N$  pixels, we compute horizontal/vertical gradient  $\boldsymbol{\alpha}$  using (4). Then, we connect gradients  $i$  and  $j$  using a positive edge with weight  $\bar{w}_{i,j}$  defined in (5). The resulting gradient line graph  $\bar{G}_k^{h,r}$  or  $\bar{G}_k^{v,c}$  has corresponding graph Laplacian matrix  $\bar{\mathbf{L}}_k^{h,r}$  or  $\bar{\mathbf{L}}_k^{v,c}$ , which is used to define GNG Laplacian  $\mathcal{L}_k^{h,r} \triangleq \mathbf{F}^\top \bar{\mathbf{L}}_k^{h,r} \mathbf{F}$  or  $\mathcal{L}_k^{v,c} \triangleq \mathbf{F}^\top \bar{\mathbf{L}}_k^{v,c} \mathbf{F}$ . Finally, the GNG Laplacians are used to define GGLR:  $\mathbf{x}^\top \mathbf{H}_k^\top \mathcal{L}_k^{h,r} \mathbf{H}_k \mathbf{x}$  or  $\mathbf{x}^\top \mathbf{G}_k^\top \mathcal{L}_k^{v,c} \mathbf{G}_k \mathbf{x}$ .

2) *Vertical/Horizontal Line Graphs for Horizontal/Vertical Gradients*: While the previous GNG Laplacians can promote PWL pixel row and column reconstruction, it is not sufficient to ensure PWP signal reconstruction. For example, consider the following  $3 \times 3$  image patch with linear pixel rows and columns, and yet the patch is not planar:

$$\mathbf{X} = \begin{bmatrix} 1 & 0 & -1 \\ 0 & 0 & 0 \\ -1 & 0 & 1 \end{bmatrix}. \quad (10)$$

Towards PWP signal reconstruction, we construct also vertical/horizontal line graphs to connect horizontal/vertical gradients as well. Specifically, denote by  $\mathbf{J}_k, \mathbf{K}_k \in \{0, 1\}^{2N \times N^2}$  the respective sampling matrix that picks out  $2N$  pixels of the  $k$ -th and  $(k+1)$ -th columns/rows from  $N^2$  entries in  $\mathbf{x}$ , *i.e.*,

$$J_{k,i,j} = \begin{cases} 1 & \text{if } i \text{ is odd and } j \text{ is } \lceil \frac{i}{2} \rceil \text{-th pixel in } k\text{-th col} \\ 1 & \text{if } i \text{ is even and } j \text{ is } \frac{i}{2} \text{-th pixel in } (k+1)\text{-th col} \\ 0 & \text{o.w.} \end{cases} \quad (11)$$

$$K_{k,i,j} = \begin{cases} 1 & \text{if } i \text{ is odd and } j \text{ is } \lceil \frac{i}{2} \rceil \text{-th pixel in } k\text{-th row} \\ 1 & \text{if } i \text{ is even and } j \text{ is } \frac{i}{2} \text{-th pixel in } (k+1)\text{-th row} \\ 0 & \text{o.w.} \end{cases} \quad (12)$$

For example,  $\mathbf{J}_1$  that picks out the 1st and 2nd columns of a  $3 \times 3$  pixel patch is

$$\mathbf{J}_1 = \begin{bmatrix} 1 & 0 & 0 & 0 & 0 & 0 & 0 & 0 & 0 \\ 0 & 1 & 0 & 0 & 0 & 0 & 0 & 0 & 0 \\ 0 & 0 & 0 & 1 & 0 & 0 & 0 & 0 & 0 \\ 0 & 0 & 0 & 0 & 1 & 0 & 0 & 0 & 0 \\ 0 & 0 & 0 & 0 & 0 & 0 & 1 & 0 & 0 \\ 0 & 0 & 0 & 0 & 0 & 0 & 0 & 1 & 0 \\ 0 & 0 & 0 & 0 & 0 & 0 & 0 & 0 & 1 \end{bmatrix}. \quad (13)$$

We correspondingly define a new gradient operator  $\tilde{\mathbf{F}} \in \mathbb{R}^{N \times 2N}$  as a counterpart to  $\mathbf{F}$  in (3) as

$$\tilde{F}_{i,j} = \begin{cases} 1 & \text{if } j \text{ is odd and } i = \lceil \frac{j}{2} \rceil \\ -1 & \text{if } j \text{ is even and } i = \frac{j}{2} \\ 0 & \text{o.w.} \end{cases}. \quad (14)$$

For example, for a  $3 \times 3$  patch,  $\tilde{\mathbf{F}}$  is

$$\tilde{\mathbf{F}} = \begin{bmatrix} 1 & -1 & 0 & 0 & 0 & 0 \\ 0 & 0 & 1 & -1 & 0 & 0 \\ 0 & 0 & 0 & 0 & 1 & -1 \end{bmatrix}. \quad (15)$$

We can now construct vertical/horizontal line graphs  $\bar{\mathcal{G}}_k^{v,r}$  or  $\bar{\mathcal{G}}_k^{h,c}$  to connect horizontal/vertical gradients  $\tilde{\mathbf{F}}\mathbf{J}_k\mathbf{x}$  or  $\tilde{\mathbf{F}}\mathbf{K}_k\mathbf{x}$  with weight  $\bar{w}_{i,j}$  defined in (5). The resulting gradient graph Laplacian matrices are  $\bar{\mathbf{L}}_k^{v,r}$  and  $\bar{\mathbf{L}}_k^{h,c}$ , which are used to define GNG Laplacian  $\mathcal{L}_k^{v,r} \triangleq \tilde{\mathbf{F}}^\top \bar{\mathbf{L}}_k^{v,r} \tilde{\mathbf{F}}$  or  $\mathcal{L}_k^{h,c} \triangleq \tilde{\mathbf{F}}^\top \bar{\mathbf{L}}_k^{h,c} \tilde{\mathbf{F}}$ . Finally, the GNG Laplacians are used to define GGLR:  $\mathbf{x}^\top \mathbf{J}_k^\top \mathcal{L}_k^{v,r} \mathbf{J}_k \mathbf{x}$  or  $\mathbf{x}^\top \mathbf{K}_k^\top \mathcal{L}_k^{h,c} \mathbf{K}_k \mathbf{x}$ .

3) *Linear Image Formation Model*: Consider a standard linear image formation for observation  $\mathbf{y} \in \mathbb{R}^M$  from ground truth signal  $\mathbf{x} \in \mathbb{R}^{N^2}$ :

$$\mathbf{y} = \mathbf{Ax} + \mathbf{n} \quad (16)$$

where  $\mathbf{A} \in \mathbb{R}^{M \times N^2}$  is a degradation matrix, and  $\mathbf{n} \in \mathbb{R}^M$  is an additive noise. Different  $\mathbf{A}$ 's imply different restoration tasks: if  $\mathbf{A}$  is an identity matrix, then optimization (17) is a denoising problem; if  $\mathbf{A} \in \{0, 1\}^{M \times N^2}$  is a sampling matrix, then (17) is an interpolation problem; if  $\mathbf{A} \in \mathbb{R}^{N^2 \times N^2}$  is a low-pass blur filter, then (17) is a non-blind deblurring problem.

4) *Optimization Objective*: Given image formation model (16) and assuming noise  $\mathbf{n}$  is Gaussian, the optimization using GGLR as prior is

$$\begin{aligned} \min_{\mathbf{x}} \|\mathbf{y} - \mathbf{Ax}\|_2^2 + \mu \mathbf{x}^\top \left( \underbrace{\sum_{k=1}^N \mathbf{H}_k^\top \mathcal{L}_k^{h,r} \mathbf{H}_k + \mathbf{G}_k^\top \mathcal{L}_k^{v,c} \mathbf{G}_k}_{\mathcal{L}} \right) \mathbf{x} \\ + \tilde{\mu} \mathbf{x}^\top \left( \underbrace{\sum_{k=1}^{N-1} \mathbf{J}_k^\top \mathcal{L}_k^{v,r} \mathbf{J}_k + \mathbf{K}_k^\top \mathcal{L}_k^{h,c} \mathbf{K}_k}_{\tilde{\mathcal{L}}} \right) \mathbf{x} \end{aligned} \quad (17)$$

where  $\mu, \tilde{\mu} > 0$  are weight parameters. Importantly, note that the priors  $\mathbf{x}^\top \mathcal{L} \mathbf{x}$  and  $\mathbf{x}^\top \tilde{\mathcal{L}} \mathbf{x}$  are sums of GGLR terms; we leverage this fact when introducing a variable number of auxiliary variables in the objective in the sequel.

### B. Plug-and-Play GGLR

Given that objective (17) is convex ( $\mathcal{L}$  and  $\tilde{\mathcal{L}}$  are provably PSD) and differentiable w.r.t. variable  $\mathbf{x}$ , one can compute solution  $\mathbf{x}^*$  by solving the linear system:

$$(\mathbf{A}^\top \mathbf{A} + \mu \mathcal{L} + \tilde{\mu} \tilde{\mathcal{L}}) \mathbf{x}^* = \mathbf{A}^\top \mathbf{y}. \quad (18)$$

See [20] for sufficient conditions when  $\mathbf{A}^\top \mathbf{A} + \mu \mathcal{L} + \tilde{\mu} \tilde{\mathcal{L}}$  is positive definite (PD) and thus invertible. One can compute  $\mathbf{x}^*$  in (18) efficiently using *conjugate gradient* (CG) without matrix inverse [49]—complexity of CG is linear assuming coefficient matrix  $\mathbf{A}^\top \mathbf{A} + \mu \mathcal{L} + \tilde{\mu} \tilde{\mathcal{L}}$  is sparse, symmetric and PD. Instead, to induce a richer set of network parameters for end-to-end optimization after unrolling (to be discussed in Section V), we intentionally introduce auxiliary variables to the objective (17) before solving the multi-variable optimization via an ADMM algorithm [22].

1) *ADMM (single auxiliary variable)*: We first introduce one auxiliary variable  $\mathbf{z}$  and constraint  $\mathbf{x} = \mathbf{z}$ , so that (17) can be rewritten using the augmented Lagrangian method as

$$\min_{\mathbf{x}, \mathbf{z}} \|\mathbf{y} - \mathbf{Ax}\|_2^2 + \mathbf{z}^\top (\mu \mathcal{L} + \tilde{\mu} \tilde{\mathcal{L}}) \mathbf{z} + \boldsymbol{\lambda}^\top (\mathbf{x} - \mathbf{z}) + \frac{\rho}{2} \|\mathbf{x} - \mathbf{z}\|_2^2 \quad (19)$$

where  $\boldsymbol{\lambda} \in \mathbb{R}^N$  is a Lagrange multiplier vector, and  $\rho > 0$  is a weight parameter. To optimize (19), we minimize variables  $\mathbf{x}$  and  $\mathbf{z}$  alternately and update  $\boldsymbol{\lambda}$  until solution  $(\mathbf{x}, \mathbf{z}, \boldsymbol{\lambda})$  converge; *i.e.*, we solve the following sub-problems at iteration  $k$ :

$$\mathbf{x}^{(k+1)} = \arg \min_{\mathbf{x}} \|\mathbf{y} - \mathbf{Ax}\|_2^2 + \frac{\rho}{2} \|\mathbf{x} - \hat{\mathbf{x}}^{(k)}\|_2^2 \quad (20)$$

$$\mathbf{z}^{(k+1)} = \arg \min_{\mathbf{z}} \mathbf{z}^\top (\mu \mathcal{L} + \tilde{\mu} \tilde{\mathcal{L}}) \mathbf{z} + \frac{\rho}{2} \|\mathbf{z} - \hat{\mathbf{z}}^{(k)}\|_2^2 \quad (21)$$

$$\hat{\boldsymbol{\lambda}}^{(k+1)} = \hat{\boldsymbol{\lambda}}^{(k)} + (\mathbf{x}^{(k+1)} - \mathbf{z}^{(k+1)}) \quad (22)$$

where

$$\hat{\boldsymbol{\lambda}}^{(k)} = (1/\rho) \boldsymbol{\lambda}^{(k)}, \hat{\mathbf{x}}^{(k)} = \mathbf{z}^{(k)} - \hat{\boldsymbol{\lambda}}^{(k)}, \hat{\mathbf{z}}^{(k)} = \mathbf{x}^{(k+1)} + \hat{\boldsymbol{\lambda}}^{(k)}. \quad (23)$$

(20) is a least-square problem independent of signal priors. (22) is a term-by-term update equation. (21) is a denoising problem for  $\mathbf{z}$  using GGLR as prior. Because we adopt GGLR as prior for the denoising problem in (21), we call the procedure to iteratively solve (20), (21) and (22) **PnP GGLR**.

2) *Solving Linear Systems via CG*: We use CG [49] to solve linear systems for  $\mathbf{x}^{(k+1)}$  in (20) and  $\mathbf{z}^{(k+1)}$  in (21):

$$(2\mathbf{A}^\top \mathbf{A} + \rho \mathbf{I}_N) \mathbf{x}^{(k+1)} = 2\mathbf{A}^\top \mathbf{y} + \rho \hat{\mathbf{x}}^{(k)} \quad (24)$$

$$(\mathbf{I}_N + \frac{2\mu}{\rho} \mathcal{L} + \frac{2\tilde{\mu}}{\rho} \tilde{\mathcal{L}}) \mathbf{z}^{(k+1)} = \hat{\mathbf{z}}^{(k)}. \quad (25)$$

Focusing on (24), we solve for  $\mathbf{x}^{(k+1)}$  iteratively. Specifically, for each iteration  $t$ , we update solution  $\mathbf{x}_{t+1}$ , residual  $\mathbf{r}_{t+1}$  and search direction  $\mathbf{p}_{t+1}$  as

$$\mathbf{x}_{t+1} = \mathbf{x}_t + \alpha_t \mathbf{p}_t \quad (26)$$

$$\mathbf{r}_{t+1} = \mathbf{r}_t - \alpha_t (2\mathbf{A}^\top \mathbf{A} + \rho \mathbf{I}_N) \mathbf{p}_t \quad (27)$$

$$\mathbf{p}_{t+1} = \mathbf{r}_{t+1} + \beta_t \mathbf{p}_t \quad (28)$$

where *step size*  $\alpha_t$  and *momentum*  $\beta_t$  are computed as

$$\alpha_t = \frac{\mathbf{r}_t^\top \mathbf{r}_t}{\mathbf{p}_t^\top (2\mathbf{A}^\top \mathbf{A} + \rho \mathbf{I}_N) \mathbf{p}_t}, \quad \beta_t = \frac{\mathbf{r}_{t+1}^\top \mathbf{r}_{t+1}}{\mathbf{r}_t^\top \mathbf{r}_t}. \quad (29)$$

Solving for  $\mathbf{z}^{(k+1)}$  in (25) can be done using CG similarly.

3) *ADMM (multiple auxiliary variables)*: We generalize the above ADMM optimization framework to the case where multiple auxiliary variables are introduced. Define  $\mathbf{z}$  and  $\tilde{\mathbf{z}}$  as auxiliary variables for the two GGLR summations in (17). The augmented Lagrangian optimization objective (19) thus becomes

$$\begin{aligned} \min_{\mathbf{x}, \mathbf{z}, \tilde{\mathbf{z}}} & \|\mathbf{y} - \mathbf{Ax}\|_2^2 + \mu \mathbf{z}^\top \mathcal{L} \mathbf{z} + \boldsymbol{\lambda}^\top (\mathbf{x} - \mathbf{z}) + \frac{\rho}{2} \|\mathbf{x} - \mathbf{z}\|_2^2 \\ & + \tilde{\mu} \tilde{\mathbf{z}}^\top \tilde{\mathcal{L}} \tilde{\mathbf{z}} + \tilde{\boldsymbol{\lambda}}^\top (\mathbf{x} - \tilde{\mathbf{z}}) + \frac{\tilde{\rho}}{2} \|\mathbf{x} - \tilde{\mathbf{z}}\|_2^2 \end{aligned} \quad (30)$$

with three optimization variables. Similar optimization subroutines as (20), (21) and (22) can be written to compute  $\mathbf{x}^{(k+1)}$ ,  $\mathbf{z}^{(k+1)}$ ,  $\tilde{\mathbf{z}}^{(k+1)}$  and update  $\boldsymbol{\lambda}^{(k+1)}$ ,  $\tilde{\boldsymbol{\lambda}}^{(k+1)}$  in order in iteration  $k$ . See Appendix C for details.

We can generalize further and define auxiliary variables  $\mathbf{z}_r$ ,  $\mathbf{z}_c$ ,  $\tilde{\mathbf{z}}_r$  and  $\tilde{\mathbf{z}}_c$  corresponding to GGLR partial sums in (17):  $\mathbf{H}_k^\top \mathcal{L}_k^{h,r} \mathbf{H}_k$ 's,  $\mathbf{G}_k^\top \mathcal{L}_k^{v,c} \mathbf{G}_k$ 's,  $\mathbf{J}_k^\top \mathcal{L}_k^{v,r} \mathbf{J}_k$ 's and  $\mathbf{K}_k^\top \mathcal{L}_k^{h,c} \mathbf{K}_k$ 's. This again leads to an iterative ADMM optimization procedure similar to one discussed earlier.

## V. UNROLLING PLUG-AND-PLAY GGLR

### A. Unrolled Network Architecture

For a given ADMM algorithm with one or more auxiliary variable  $\mathbf{z}$  corresponding to GGLR subset sums, we unroll it into  $K$  GGLR layers as shown in Fig. 2. Each GGLR layer has the same structure and parameters. Specifically, each layer contains a graph learning module and a GGLR-based optimization module. For the single auxiliary variable case, a GGLR-based optimization module contains the  $k$ -th iteration of (24) and (25). To learn edge weights from data to define GNG Laplacians, we adopt a shallow CNN<sub>f</sub> network to learn low-dimensional feature vectors  $\mathbf{f}_i \in \mathbb{R}^K$  per pixel  $i$ , and then compute horizontal and vertical gradients to establish edge weights in (5). The use of a shallow CNN for low-dimensional feature learning towards the construction of a similarity graph contributes to network parameter reduction. Further, in each GGLR-based optimization module, we employ a CNN<sub>y</sub> network to pre-filter the image  $\mathbf{z}^{(k)}$ , following the approach in [40]. Parameters  $\rho$ ,  $\mu$  and  $\tilde{\mu}$  in (24) and (25) are trainable parameters in the unrolled network.

We unroll the iterative CG algorithm for solving linear system (24) into  $L$  neural layers, where  $\alpha_{\mathbf{x}} = \{\alpha_0, \dots, \alpha_{L-1}\}$  and  $\beta_{\mathbf{x}} = \{\beta_0, \dots, \beta_{L-2}\}$  are CG parameters learned from data. Similarly, parameter sets  $\alpha_{\mathbf{z}}$  and  $\beta_{\mathbf{z}}$  are separate CG

parameters learned for solving linear system (25). As shown in Fig. 2(c), each unrolled CGD layer includes  $L$  iterations of (26) to (28). The blue lines denote computation of  $\mathbf{x}$ , the black lines denote computation of  $\mathbf{p}$ , and the green lines denote computation of  $\mathbf{r}$ .

Similarly done in [41], the input to the algorithm is a degraded observed image  $\mathbf{z}^{(0)} = \mathbf{y}$  and  $\hat{\boldsymbol{\lambda}}^{(0)} = \mathbf{0}$ . After the unrolled  $K$  layers, we obtain the reconstruction signal  $\mathbf{x}^K$ . The GGLRLayer<sub>k</sub> uses the signal after  $k-1$  iterations  $\mathbf{z}^{(k-1)}$ ,  $\hat{\boldsymbol{\lambda}}^{(k-1)}$  and a set of learned parameters  $\boldsymbol{\Theta}^k = \{\sigma_a^{(k)}, \sigma_f^{(k)}, \rho^{(k)}, \mu^{(k)}, \tilde{\mu}^{(k)}, \theta_f^{(k)}, \theta_y^{(k)}, \alpha_{\mathbf{x}}^{(k)}, \beta_{\mathbf{x}}^{(k)}, \alpha_{\mathbf{z}}^{(k)}, \beta_{\mathbf{z}}^{(k)}\}$  as input, where  $\theta_f^{(k)}$  and  $\theta_y^{(k)}$  denote the parameter sets of CNN<sub>f</sub> and CNN<sub>y</sub>, respectively.

To effectively train the proposed unrolling PnP GGLR (UPnP GGLR), we evaluate the difference between the recovered image  $\mathbf{x}^K$  and the ground-truth image  $\mathbf{x}^{gt}$  after the last GGLR layer. Specifically, we compute the partial derivative of the *mean square error* (MSE) between  $\mathbf{x}^{gt}$  and  $\mathbf{x}^K$  and back-propagate it to update parameters  $\{\boldsymbol{\Theta}^1, \dots, \boldsymbol{\Theta}^K\}$  for  $T$  training patches:

$$\mathcal{L}_{\text{MSE}}(\boldsymbol{\Theta}^1, \dots, \boldsymbol{\Theta}^K) = \frac{1}{T} \sum_{i=1}^T \|\mathbf{x}_i^K - \mathbf{x}_i^{gt}\|_2^2. \quad (31)$$

### B. Self-Attention Operator in Transformer

We argue that the periodically inserted graph learning module in our unrolled network is akin to the self-attention mechanism [23] in a conventional transformer architecture [24]. We first review the typical self-attention operator, defined using a linearly-transformed dot product. Denote by  $\mathbf{x}_i \in \mathbb{R}^B$  an input *embedding* for token  $i$  of  $N$  total input tokens. The *affinity*  $e(i, j)$  between tokens  $i$  and  $j$ —a measure of how relevant key token  $i$  is to query token  $j$ —is defined as the dot product between linearly-transformed  $\mathbf{Kx}_i$  and  $\mathbf{Qx}_j$ :

$$e(i, j) = (\mathbf{Qx}_j)^\top (\mathbf{Kx}_i). \quad (32)$$

where  $\mathbf{Q}, \mathbf{K} \in \mathbb{R}^{B \times B}$  are respectively the *query* and *key* matrices—dense matrices learned from data.

Commonly, using a non-linear function called *softmax*, *attention weight*  $a_{i,j}$  is computed as

$$a_{i,j} = \frac{\exp(e(i, j))}{\sum_{l=1}^N \exp(e(i, l))}. \quad (33)$$

Besides converting an input set of real values  $e(i, j)$ 's to positive values  $a_{i,j}$ 's, softmax also normalizes  $a_{i,j}$ 's so that they sum to 1.

Using weights  $a_{i,j}$ 's, we compute the output embedding  $\mathbf{y}_i$  for token  $i$  using a *value* matrix  $\mathbf{V} \in \mathbb{R}^{B \times B}$ , another dense matrix learned from data, as

$$\mathbf{y}_i = \sum_{l=1}^N a_{i,l} \mathbf{x}_l \mathbf{V}. \quad (34)$$

The term “self-attention” conveys the notion that output embeddings are computed using input embeddings. A sequence of embedding-to-embedding mappings composes a transformer, defined by the corresponding learned matrices,  $\mathbf{Q}$ ,  $\mathbf{K}$  and  $\mathbf{V}$

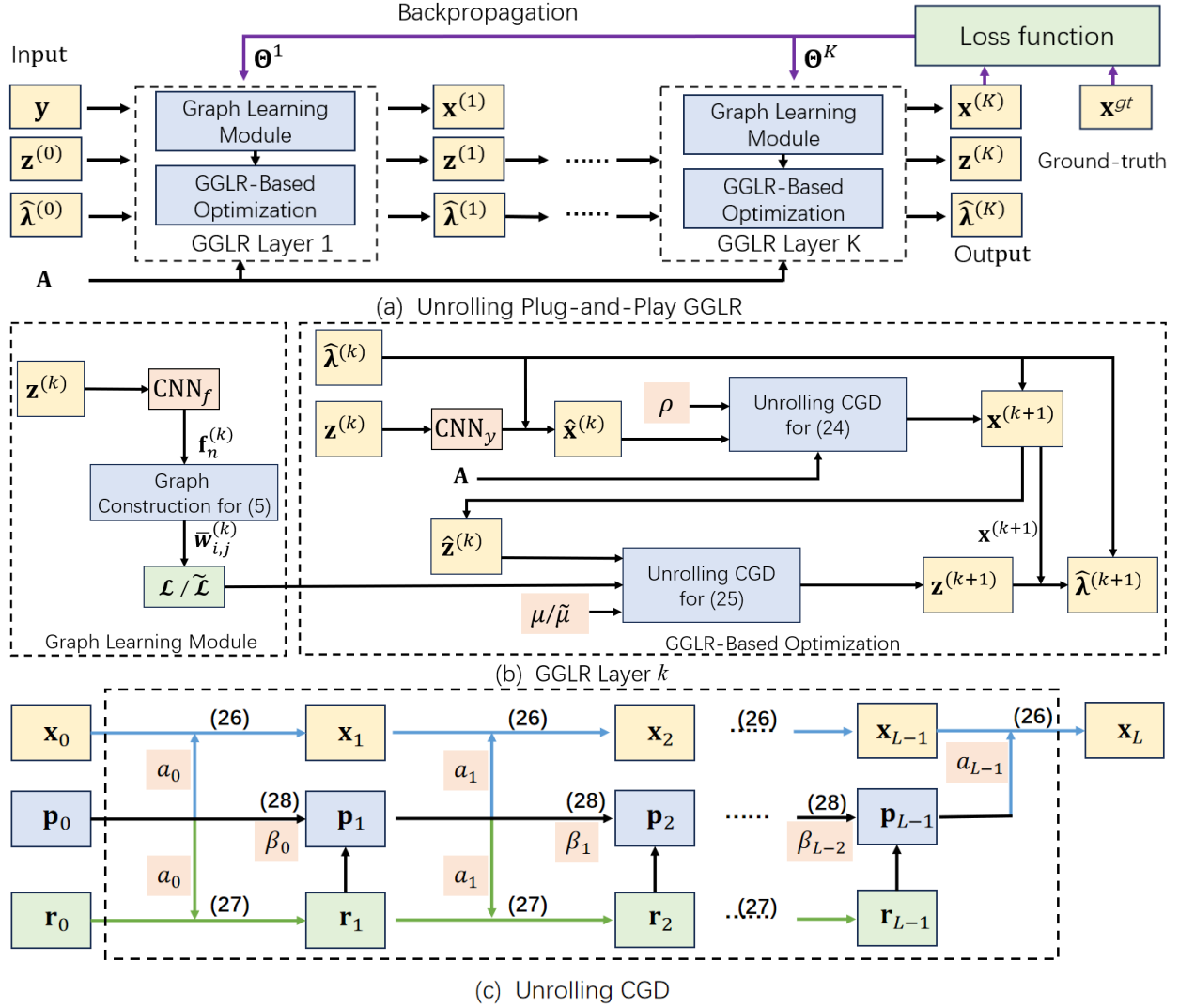


Fig. 2. Overview of the proposed architecture. (a) UPnPGLR composed of multiple GGLR Layers, (b) Block diagram of GGLR Layer  $k$ , (c) Unrolling CGD.

in each mapping. Note that one can extend the framework to *multi-head* attention, when we use multiple query and key matrices  $\mathbf{Q}^{(m)}$  and  $\mathbf{K}^{(m)}$  to compute different weights  $a_{i,j}^{(m)}$ 's for the same input embeddings  $\mathbf{x}_i$  and  $\mathbf{x}_j$ . In this case, we compute output  $\mathbf{y}_i$  as the average of these multi-head attention weights  $a_{i,l}^{(m)}$ 's.

### C. Computation of Normalized Graph Edge Weights

We next examine how we compute *normalized* edge weights  $\tilde{w}_{i,j}$ 's to define GLR for the gradient graph  $\tilde{\mathcal{G}}$ . Using CNN, we compute a low-dimensional *feature vector*  $\mathbf{f}_i \in \mathbb{R}^D$  for each node  $i$  from embedding  $\mathbf{x}_i \in \mathbb{R}^B$  as  $\mathbf{f}_i = F(\mathbf{x}_i)$ , where  $D \ll B$ . To compute *unnormalized* edge weight  $w_{i,j}$  between nodes  $i$  and  $j$ , we first compute the squared Euclidean distance  $d(i,j) = \|\mathbf{f}_i - \mathbf{f}_j\|_2^2$  in feature space, and  $w_{i,j} = \exp(-d(i,j))$ . Then, *normalized* edge weight  $\tilde{w}_{i,j}$  is computed as

$$\tilde{w}_{i,j} = \frac{w_{i,j}}{\sum_l w_{i,l}} = \frac{\exp(-d(i,j))}{\sum_l \exp(-d(i,l))}. \quad (35)$$

In matrix form, the *random-walk graph Laplacian* is thus  $\tilde{\mathbf{L}} = \bar{\mathbf{D}}^{-1}\tilde{\mathbf{L}}$ . Since  $\tilde{\mathbf{L}}$  is not symmetric, instead of conventional

GLR, we define a variant of GLR based on the random-walk Laplacian [13]:

$$\alpha^\top \tilde{\mathbf{L}}^\top \tilde{\mathbf{L}} \alpha = \mathbf{x}^\top \underbrace{\mathbf{F}^\top \tilde{\mathbf{L}}^\top \tilde{\mathbf{L}} \mathbf{F}}_{\tilde{\mathcal{L}}} \mathbf{x} = \mathbf{x}^\top \tilde{\mathcal{L}} \mathbf{x}. \quad (36)$$

Unlike (6), GGLR in (36) is defined using a normalized Laplacian, and yet computes to zero for constant gradient—i.e.,  $\mathbf{1}^\top \tilde{\mathbf{L}}^\top \tilde{\mathbf{L}} \mathbf{1} = 0$ , as expected for a linear signal.

**Comparison to Self-Attention Operator:** We see how the computation of edge weights (35) is akin to the computation of attention weights in (33). Specifically, *interpreting the negative squared Euclidean distance  $-d(i,j)$  as affinity  $e(i,j)$ , normalized edge weights  $\tilde{w}_{i,j}$ 's in (35) are essentially the same as attention weights  $a_{i,j}$ 's in (33)*. However,  $-d(i,j)$ 's are computed using shallow CNNs that are more compact than dense query and key matrices,  $\mathbf{Q}$  and  $\mathbf{K}$ . Further, given a graph  $\mathcal{G}$  specified by  $\tilde{\mathcal{L}}$ , the restored signal  $\mathbf{x}^*$  is a low-pass filtered  $(\mathbf{A}^\top \mathbf{A} + \mu \tilde{\mathcal{L}})^{-1}$  output of  $\mathbf{A}^\top \mathbf{y}$  in linear system (18) (computed via our proposed family of unrolled PnP-GGLR algorithms), while the output embedding  $\mathbf{y}_i$  in a conventional transformer requires dense value matrix  $\mathbf{V}$  in (34). Thus, each

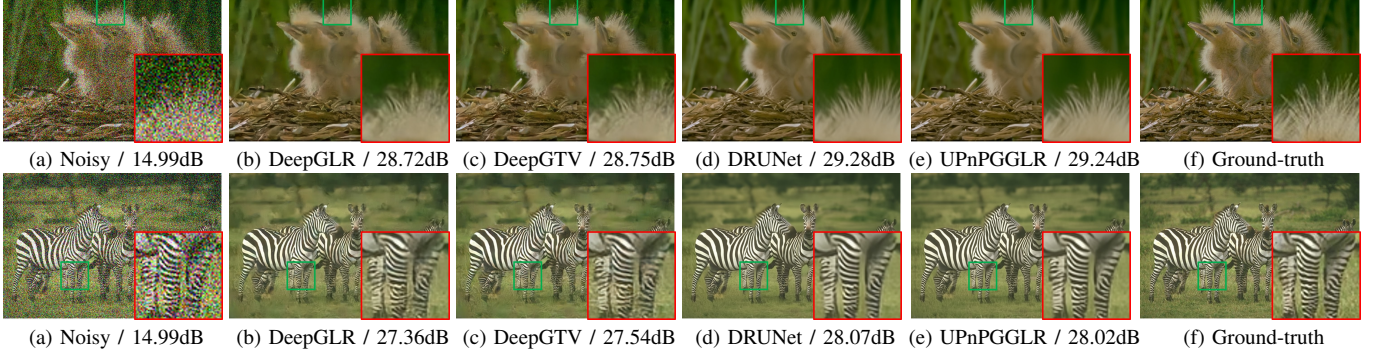


Fig. 3. Color image denoising results of different methods on image “163085” and image “253027” from CBSD68 dataset with noise level 50.

graph learning module corresponds to the learning of attention weights, while the GGLR-based optimization corresponds to parameter-efficient attention-based filtering.

## VI. EXPERIMENTS

### A. Experimental Setup

We set the number of GGLR layers to  $K = 10$  and the number of CGD layers to  $L = 10$ . The  $\text{CNN}_f$  consists of 6 convolution layers. The first layer has 3 input channels and 32 output channels. The last layer has 32 input channels and 3 output channels. We use a  $\text{ReLU}(\cdot)$  activation function after every convolutional layer. The  $\text{CNN}_y$  consists of 4 convolutional layers using a residual learning structure. For both training and testing, the patch size is set to  $36 \times 36$ , and the patches are extracted from images in an overlapped sliding window, where the stride is set to 32. In each experiment, we train our proposed UPnPGLR model for 200 epochs using stochastic gradient descent (SGD). The batch size is set to 16, and the learning rate is set to  $1e^{-4}$ . The proposed model is implemented in PyTorch and trained on an Nvidia 3090 GPU. We evaluate the performance using two common image metrics, peak signal-to-noise ratio (PSNR), and structural similarity index measure (SSIM) [50], on the test images.

Parameters  $\sigma_a$  and  $\sigma_f$  in (5) were initialized to 0.01, parameters  $\mu$  and  $\tilde{\mu}$  were initialized to 0.3, and parameter  $\rho$  was initialized to 1. Constraints were imposed on  $\mu$ ,  $\tilde{\mu}$  and  $\rho$  to ensure their non-negativity. These constraints not only align with the mathematical contexts of different terms in the optimization objective, but also contribute to the stability and robustness of the training process. As the training progressed through iterations, these parameters eventually converged to fixed values. A detailed discussion is presented in Section VI-E.

We note that though in principle the same pre-trained GGLR-based denoiser can be reused for different settings, towards optimal performance, we retrained our model parameters for different definitions of  $\mathbf{A}$ , given that the statistics for different applications differ in general.

To validate the importance of the graph learning module (periodic learning of attention weights), we introduced a variant named UPnPGLR-S, where a single fixed (but optimized) graph is used for GGLR optimization across all layers. We

TABLE I  
AVERAGE PSNR(dB) RESULTS OF DIFFERENT METHODS FOR NOISE LEVELS 15, 25, AND 50 ON CBSD68 [51] DATASET.

Method	Paras(M)	CBSD68 [51]		
		$\sigma = 15$	$\sigma = 25$	$\sigma = 50$
CBM3D [37]	-	33.49/0.922	30.68/0.867	27.35/0.763
TWSC [38]	-	33.41/0.918	30.64/0.867	27.43/0.763
NSS [39]	-	33.33/0.918	30.76/0.868	27.61/0.769
CDnCNN [26]	0.56	33.90/0.929	31.22/0.883	27.95/0.790
IRCNN [52]	4.75	33.87/0.928	31.18/0.882	27.86/0.789
FFDNet [27]	0.67	33.85/0.929	31.22/0.883	27.98/0.792
DeepGLR [40]	0.93	33.75/0.926	31.13/0.881	27.86/0.791
DeepGTV [41]	0.10	33.80/0.927	31.08/0.879	27.90/0.791
DRUNet [53]	32.64	34.30/0.934	31.69/0.893	28.51/0.810
Restormer [25]	26.11	<b>34.39/0.935</b>	<b>31.78/0.894</b>	<b>28.59/0.813</b>
UPnPGLR-S	<b>0.09</b>	33.91/0.930	31.19/0.882	27.95/0.792
UPnPGLR	0.23	34.15/0.932	31.42/0.889	28.18/0.802

will demonstrate that UPnPGLR outperforms UPnPGLR-S generally, thereby demonstrating the importance of the graph learning module in enhancing restoration performance.

### B. Image Denoising

For additive white Gaussian noises (AWGN) denoising, we set the degradation matrix  $\mathbf{A}$  in (16) to identity. We used BSDS500 [51] for evaluation as done in [26]. It consists of 432 training images and 68 test images. They were corrupted by AWGN of standard deviation  $\sigma$  ranging from 5 to 55.

We first compare our proposed UPnPGLR model with CBM3D [37], TWSC [38], NSS [39], CDnCNN [26], IRCNN [52], FFDNet [27], DeepGLR [40], DeepGTV [41], DRUNet [53], Restormer [25]. Note that CBM3D, TWSC and NSS are pure model-based methods, and thus do not require data-driven parameter tuning. DeepGLR and DeepGTV are hybrid methods that combine CNNs with graph smoothness priors. Restormer is a method based on transformers, whereas DRUNet uses a pure CNN model as a denoiser. Both Restormer and DRUNet require a substantial number of network parameters and are prone to overfitting.

To evaluate the proposed method, we conducted comparative experiments at noise levels  $\sigma = \{10, 25, 50\}$ . The PSNR and SSIM results are shown in Table I. While model-based methods TWSC [38] and NSS [39] are more interpretable, their denoising performances are glaringly inferior compared to SOTA DNNs, due to their overly restrictive assumed models. We observe that Restormer achieves the best PSNR results on AWGN, but outperforming our proposed UPnPGLR only

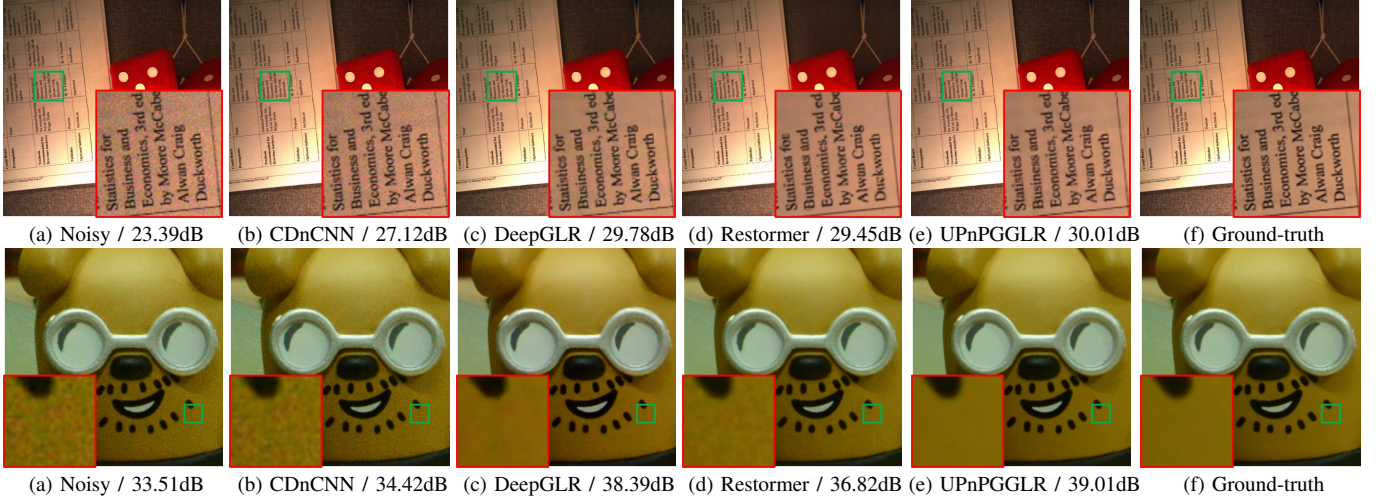


Fig. 4. Visual comparison of cross-domain generalization. Note that the proposed UPnPGLR is trained on Gaussian white noises for image denoising and generalizes well to real image denoising.

TABLE II

EVALUATION OF CROSS-DOMAIN GENERALIZATION FOR REAL IMAGE DENOISING ON RENOIR [54] AND NAM-CC15 [55] DATASETS. THE BEST RESULTS ARE HIGHLIGHTED IN BOLDFACE.

Dataset	Method	CDnCNN [26]	IRCNN [52]	FFDNet [27]	DeepGLR [40]	DeepGTV [41]	DRUNet [53]	Restormer [25]	UPnPGLR-S	UPnPGLR
RENOIR [54]	PSNR	26.79	25.77	29.19	30.25	30.14	29.81	29.55	30.26	<b>30.38</b>
	SSIM	0.638	0.651	0.762	0.809	0.808	0.784	0.780	0.809	<b>0.814</b>
Nam-CC15 [55]	PSNR	33.86	35.68	34.00	35.85	35.98	35.52	35.32	36.06	<b>36.26</b>
	SSIM	0.864	0.932	0.906	0.935	0.932	0.927	0.921	0.934	<b>0.939</b>

TABLE III

THE IMPACT OF THE NUMBER OF AUXILIARY VARIABLES ON MODEL PERFORMANCE.

Auxiliary variables	Paras(M)	AWDN denoising on CBSD68 [51]			Interpolation on set5 [56]			Deblurring on set6 [52]	
		$\sigma = 15$	$\sigma = 25$	$\sigma = 50$	20%	50%	80%	Kernel 1	Kernel 2
DeepGLR [40]	0.93	33.75/0.926	31.13/0.881	27.86/0.791	38.92/0.981	33.75/0.948	27.48/0.843	33.28/0.924	33.53/0.928
DeepGTV [41]	<b>0.10</b>	33.80/0.927	31.08/0.879	27.90/0.791	38.85/0.980	33.65/0.948	27.42/0.842	34.17/0.923	33.42/0.928
GGGLR	0.23	33.92/0.929	31.27/0.883	28.01/0.792	39.61/0.982	34.53/0.951	28.62/0.869	34.38/0.937	34.04/0.934
UPnPGLR-O	0.23	34.08/0.931	31.35/0.888	28.11/0.801	39.79/0.983	34.72/ <b>0.952</b>	28.87/0.874	34.51/0.940	34.12/0.936
UPnPGLR-T	0.23	34.12/0.931	31.38/ <b>0.889</b>	28.15/ <b>0.802</b>	39.84/0.983	34.78/ <b>0.952</b>	28.94/0.876	34.54/ <b>0.941</b>	34.15/0.936
UPnPGLR-F	0.23	<b>34.15/0.932</b>	<b>31.42/0.889</b>	<b>28.18/0.802</b>	<b>39.88/0.984</b>	<b>34.81/0.952</b>	<b>28.98/0.877</b>	<b>34.57/0.941</b>	<b>34.18/0.937</b>

slightly. However, Restormer incurs a significant larger number of parameters—UPnPGLR employs less than 1% of the parameters in Restormer. Compared to similar hybrid models such as DeepGLR and DeepGTV, UPnPGLR achieves noticeably better performance. Further, UPnPGLR achieves better performance than UPnPGLR-S, demonstrating the importance of the graph learning module in denoising.

A visual comparison of the models is shown in Fig. 3. We observe that DeepGLR and DeepGTV fail to fully remove noises in the restored images, while UPnPGLR obtains more visually satisfactory results—the restored images appear less blocky and more natural. Moreover, our network performs comparably to generic DNNs like DRUNet while using fewer than 1% of the parameters.

1) *Robustness to Covariate Shift*: The robustness of our approach is evaluated in terms of its cross-domain generalization ability. Specifically, the evaluation is conducted on the real noise dataset RENOIR [54] and Nam-CC15 [55], using the model trained for AWGN of standard deviation  $\sigma \in [5, 55]$ . The RENOIR dataset consists of 10 high-resolution real low-light noisy images and their corresponding noise-free versions. The Nam-CC15 dataset includes 15 noisy images of size  $512 \times 512$  captured by Canon 5D Mark III, Nikon D600, and Nikon D800 cameras.

We compare our proposed UPnPGLR model only with top-performing denoisers in Table I: CDnCNN [26], IRCNN [52], FFDNet [27], DeepGLR [40], DeepGTV [41], DRUNet [53] and Restormer [25]. PSNR and SSIM results are shown in Table II. We observe that UPnPGLR surpasses Restormer by 0.83dB PSNR on the RENOIR dataset and by 0.94dB PSNR on the Nam-CC dataset. However, Restormer provides better results in Gaussian noise removal, as we saw in Table I. This indicates that Restormer is overfitted to Gaussian noise and fails to generalize to real noise, whereas UPnPGLR provides satisfactory denoising results in both cases. Compared to similar hybrid models such as DeepGLR and DeepGTV, UPnPGLR achieves the best PSNR results on both real image noise datasets. Fig. 4 shows representative visual denoising results of the RENOIR and Nam-CC15 datasets. We observe that the competing methods fail to remove the real noise in the restored images, whereas the proposed method provides better visual quality.

Fig. 6(a) shows the performance of different methods under covariate shift. The models were trained with noise  $\sigma = 15$  on the BSDS500 dataset and tested at various noise levels. As the noise level increases, the performance of all models decreases. However, our method shows a noticeable improvement in robustness to covariate shift over competitors.

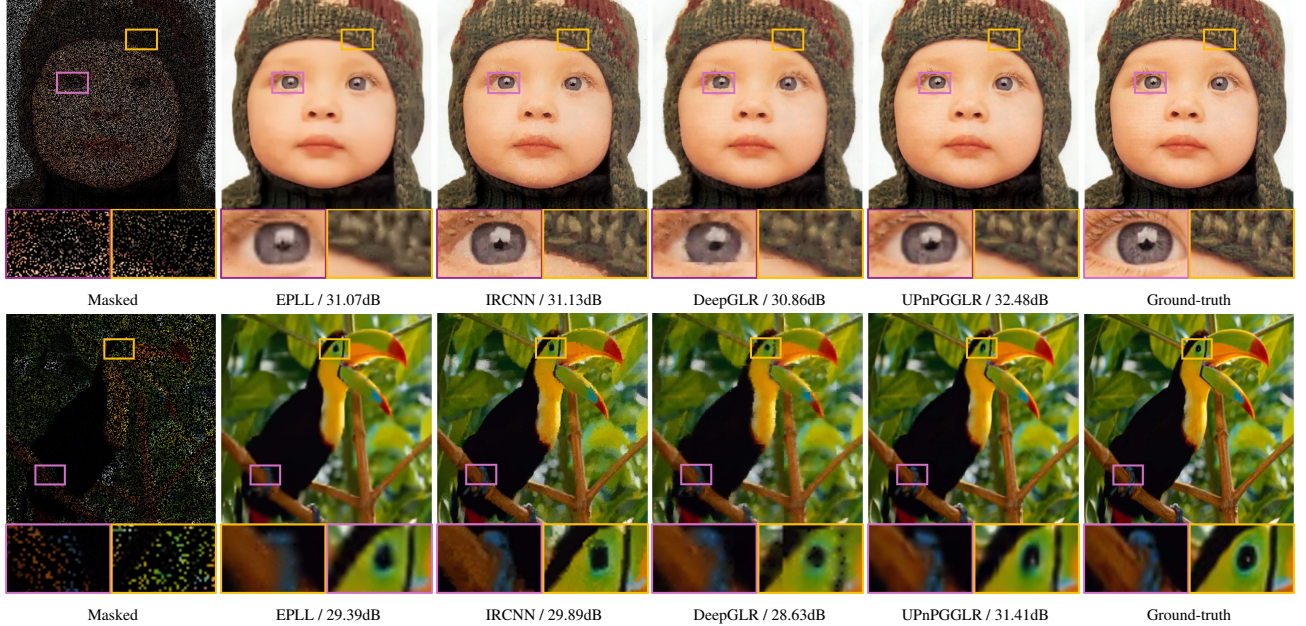


Fig. 5. Visual comparision for interpolating 80% of missing pixels on the Set5 dataset [56]. Interpolation by UPnPGLR looks less blocky and more natural.

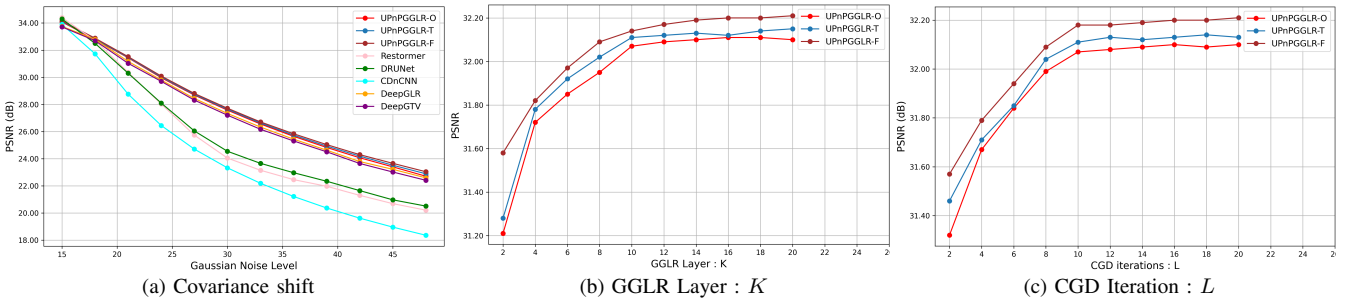


Fig. 6. Image quality in PSNR versus the number of GGLR layers and CGD iterations on RENOIR dataset.

2) *Effects of Auxiliary Variables*: We compare different variants of UPnPGLR algorithms with different number of auxiliary variables for different restoration scenarios: denoising, interpolation, and non-blind deblurring (the datasets will be introduced in the sequel). In Table III, GGLR denotes the model of solving the linear system (18) directly by unrolling CGD, while UPnPGLR-O, UPnPGLR-T, and UPnPGLR-F denote the ADMM algorithm with one auxiliary variable ( $\mathbf{z}$ ), two auxiliary variables ( $\mathbf{z}_r$ ,  $\mathbf{z}_c$ ), and four auxiliary variables ( $\mathbf{z}_r$ ,  $\mathbf{z}_c$ ,  $\tilde{\mathbf{z}}_r$ ,  $\tilde{\mathbf{z}}_c$ ), respectively. The first and second rows in Table III show the performance of DeepGLR and DeepGTV in image restoration. We see that the performance of GGLR is superior to that of DeepGLR and DeepGTV. From the fourth to sixth rows of the table, we see a progressive improvement in performance by gradually introducing more auxiliary variables. This improvement is attributed to the network's ability to learn more parameters along individual dimensions. Note that introducing additional auxiliary variables only marginally increases the parameter count. Further, ADMM induces a structured and interpretable optimization process by decoupling the problem into simpler sub-problems focusing on minimization of individual terms. This structured approach not only enhances the clarity of the optimization process but also

contributes to the overall effectiveness of the proposed method.

3) *Ablation Study*: We investigate the impact of the number of GGLR layers and the iteration numbers of CGD. Experiments are conducted on the RENOIR dataset [54] following recent works [40], [41]. The images are split into two sets for training and testing, with each set containing five images. Fig. 6(b) shows the average PSNR results of the proposed UPnPGLR with different GGLR layer numbers  $K$ , given a fixed CGD iteration number  $L = 10$ . It is evident that PSNR of UPnPGLR increases rapidly for  $K \leq 10$ , but the improvement becomes marginal for  $K > 10$ . Fig. 6(c) shows the influence of the iteration numbers of GCD given  $K = 10$ . Similarly, we can see that the PSNR performance improves as the number of iterations increases. Ultimately, we set  $K = 10$  and  $L = 10$ . Additionally, we find that while increasing the number of auxiliary variables improves model performance, it has minimal impact on the selection of layers and iterations.

4) *Computational Efficiency*: We conducted experiments to compare the computational efficiency of different methods in terms of parameter count, runtime (inference time), and FLOPs. The results are summarized in Table IV. All experiments were performed on the CBSD68 denoising dataset with

TABLE IV  
PARAMETERS (IN M), RUNTIME (IN SECONDS) AND FLOPS (IN G) OF DIFFERENT METHODS ON IMAGES OF SIZE 480×320 WITH NOISE LEVEL 50.

Metric	CDnCNN [26]	IRCNN [52]	DeepGLR [40]	DeepGTV [41]	DRUNet [53]	Restormer [25]	UPnPGLR
Paras(M)	0.56	4.75	0.93	<b>0.10</b>	32.64	26.11	0.23
Runtime(Sec)	<b>0.13</b>	0.47	9.01	7.86	0.27	0.28	9.02
FLOPs(G)	102.99	28.99	8.71	<b>4.08</b>	336.58	344.35	10.43

TABLE V  
IMAGE INTERPOLATION RESULTS (PSNR/SSIM) BY DIFFERENT METHODS ON SET5 [56].

Method	EPLL [57]	IRCNN [52]	DeepGLR [40]	DeepGTV [41]	SNORE [43]	UPnPGLR-S	UPnPGLR
Paras(M)	1.65	4.75	0.93	0.10	32.64	<b>0.09</b>	0.23
20% missing	37.23/0.974	39.20/0.981	38.92/0.981	38.85/0.980	<b>40.01/0.985</b>	39.32/0.981	39.88/0.984
50% missing	33.25/0.943	33.84/0.949	33.75/0.948	33.65/0.948	34.66/ 0.951	34.37/0.950	<b>34.81/0.952</b>
80% missing	27.87/0.833	28.32/0.864	27.48/0.843	27.42/0.842	21.96/0.736	28.48/0.867	<b>28.98/0.877</b>

images of size 480×320. Our method achieves a good tradeoff between FLOPS (10.43 G) and parameter count (0.23 M). In contrast, Restormer and DRUNet require substantial parameter counts and computational resources (FLOPS).

We note that runtimes for graph-based deep unrolling schemes (*e.g.*, DeepGLR, DeepGTV, UPnPGLR) are noticeably larger. This is due to the current lack of efficient implementations of sparse matrix-vector multiplication. Addressing this software engineering challenge to improve runtime is left for future research.

### C. Image Interpolation

For image interpolation, the degradation matrix  $\mathbf{A}$  in (16) is a sampling matrix. We conducted training on the 432 images of the BSDS500 dataset [51] and tested on the Set5 dataset [56]. We compared our method against SOTA image interpolation techniques, including EPLL [57], IRCNN [52], DeepGLR [40], DeepGTV [41] and the latest plug-and-play method, SNORE [43]. The average PSNR and SSIM of the reconstructed images are shown in Table V. Notably, UPnPGLR demonstrates superior performance compared to the competing methods, particularly in scenarios with a large fraction of missing pixels. For instance, in the case of 80% pixel loss, UPnPGLR outperforms SNORE by achieving a PSNR of 28.98 dB. A representative visual comparison is shown in Fig. 5. We observe that IRCNN tends to over-smooth edges, while our method can reconstruct images with sharp edges and natural textures. *Note that UPnPGLR employs fewer than 5% of the parameters in IRCNN.*

### D. Non-Blind Image Deblurring

For non-blind image deblurring, degradation matrix  $\mathbf{A}$  in (16) is a known low-pass blur filter. The blurry images were synthesized by first applying a blur kernel and then adding additive Gaussian noise with noise level  $\sigma$ . For training, we filtered 432 images from BSDS500 [51] with the two real blur kernels from [58] and then added 1% white Gaussian noise to the images. We created a test dataset Set6 which selected six images from [52].

To evaluate the effectiveness of UPnPGLR, we compared it against four representative methods: the model-based EPLL [57] and RGTV [15], the learning-based non-blind FDN [59] and IRCNN [52], and recent plug-and-play approaches Eq.DRUNet [42] and SNORE [43]. The PSNR and SSIM of different methods are shown in Table VI. Our method achieves

superior results compared to both Eq.DRUNet and SNORE across two different blur kernels. Fig. 7 visually compares deblurred images by different methods. We observe that RGTV and FDN tend to smooth out fine details and generate color artifacts. Although IRCNN avoids color artifacts, it fails to recover fine details. In contrast, the proposed method can recover image edges and textures more naturally.

### E. Learnable Parameter Variation

The learnable parameters in our work are mainly  $\{\sigma_a^{(k)}, \sigma_f^{(k)}, \rho^{(k)}, \mu^{(k)}, \tilde{\mu}^{(k)}, \alpha_x^{(k)}, \beta_x^{(k)}, \alpha_z^{(k)}, \beta_z^{(k)}\}$ . We study the evolution of these learned parameters for further insights. We described the initialization of key learnable parameters in Section VI-A. Given the initial values, these parameters gradually converge to specific values during the training process. Fig. 8 shows the evolution of parameters  $\mu$ ,  $\tilde{\mu}$ , and  $\rho$  across iterations for the first GGLR layer. For instance, the initial values of  $\mu$  and  $\tilde{\mu}$  were set to 0.3, and both eventually converged to near 1. These parameters control the weights of the horizontal and vertical GGLR terms, respectively; their converged values are similar, reflecting their balanced contributions to the model.

## VII. CONCLUSION

Towards interpretable and lightweight deep neural nets for image restoration, we design a family of graph-based ADMM optimization algorithms by varying the number of introduced auxiliary variables and unroll them into feed-forward networks for data-driven parameter tuning. This is possible thanks to a recent graph smoothness prior GGLR (promoting PWP reconstruction) that is a sum of priors applied separately to individual pixel rows and columns of a target patch. We argue that our periodically inserted graph learning module is akin to the self-attention mechanism in a conventional transformer architecture, but by adopting shallow CNNs to learn low-dimensional feature representations, our variant is dramatically more parameter-efficient. Experimental results show that our unrolled networks perform competitively to SOTA in various image restoration tasks, while using only a small fraction of parameters. Moreover, our model demonstrates improved robustness to covariate shift.

Our proposed UPnPGLR has some limitations. First, our current framework is limited to image formation models that are linear in the form  $\mathbf{y} = \mathbf{Ax} + \mathbf{n}$ , where  $\mathbf{n}$  is an additive Gaussian noise. Formation models that are non-linear, or

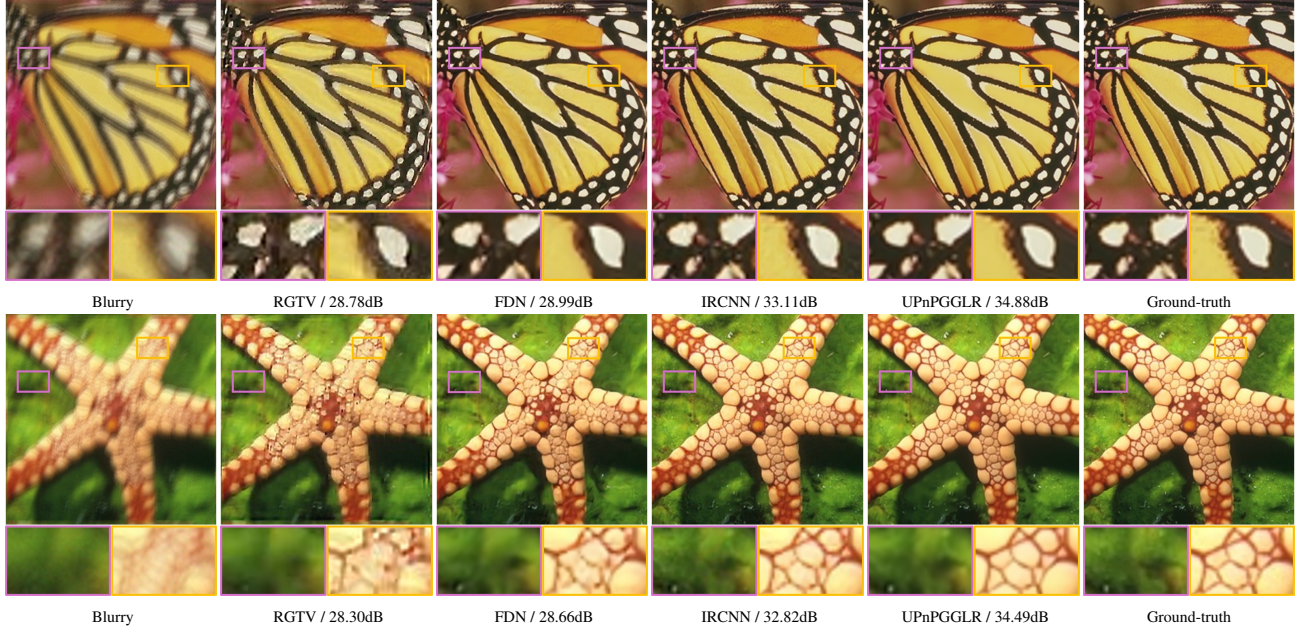


Fig. 7. Visual results comparison of different deblurring methods on Set6 dataset [52]. The blur kernel size is  $19 \times 19$  and the noise level is 2.55 (1%).

TABLE VI  
PSNR/SSIM RESULTS OF DIFFERENT METHODS ON SET6 [52] FOR IMAGE DEBLURRING.

Method	EPPLL [57]	RGTV [60]	FDN [59]	IRCNN [52]	Eq.DRUnet [42]	SNORE [43]	UPnPGLR-S	UPnPGLR
Paras(M)	1.65	-	0.39	4.75	32.64	32.64	<b>0.09</b>	0.23
Kernel 1 $19 \times 19$	27.88/0.843	28.54/0.849	28.94/0.856	33.02/0.922	29.16/0.863	31.98/0.907	34.07/0.933	<b>34.57/0.941</b>
Kernel 2 $17 \times 17$	27.56/0.840	27.98/0.845	28.53/0.851	32.43/0.911	29.23/0.865	31.76/0.904	33.98/0.932	<b>34.57/0.941</b>

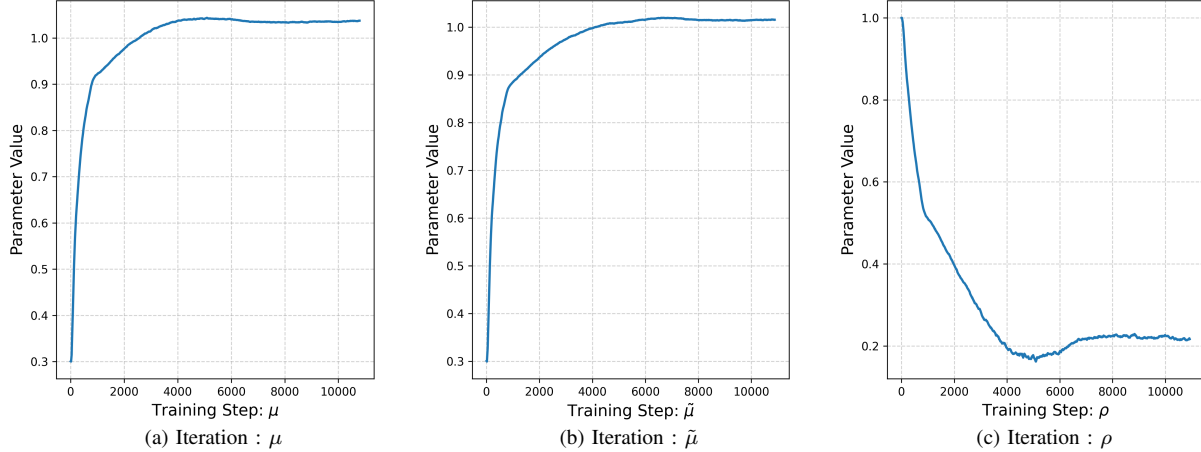


Fig. 8. Plots for ablation experiments showing the evolution of the learnable parameters  $\mu$ ,  $\tilde{\mu}$  and  $\rho$  across iterations.

with noise that are not additive Gaussian, are currently not directly applicable. Second, the inference time of our method is relatively slow. This is due to the current lack of efficient implementations of sparse matrix-vector multiplication. Future work will focus on addressing these limitations.

When denoising noise-corrupted observation  $\mathbf{y} \in \mathbb{R}^N$ , solution  $\mathbf{x}^* \in \mathbb{R}^N$  is the argument minimizing the following objective regularized using the *graph Laplacian regularizer* (GLR) [12]  $\mathbf{x}^\top \mathbf{L} \mathbf{x}$  as signal prior given graph Laplacian matrix  $\mathbf{L} \in \mathbb{R}^{N \times N}$  corresponding to a positive graph  $\mathcal{G}$ :

$$\mathbf{x}^* = \arg \min_{\mathbf{x}} \|\mathbf{y} - \mathbf{x}\|_2^2 + \mu \mathbf{x}^\top \mathbf{L} \mathbf{x} \quad (37)$$

#### A. GLR Promoting PWC Signal Reconstruction

Different from arguments in [12], [13], we argue here that iterative GLR promotes *piecewise constant* (PWC) signal reconstruction from an anisotropic diffusion perspective.

where  $\mu > 0$  is a weight parameter trading off the fidelity term and the signal prior.  $\mathbf{x}^*$  can be computed via the inverse of a positive definite (PD) matrix  $\mathbf{I}_N + \mu \mathbf{L}$ , given  $\mu > 0$  and  $\mathbf{L}$  is a provably positive semi-definite (PSD) Laplacian matrix

#### APPENDIX

to a positive graph  $\mathcal{G}$  [11]:

$$\mathbf{x}^* = (\mathbf{I}_N + \mu \mathbf{L})^{-1} \mathbf{y} \stackrel{(a)}{\approx} \sum_{m=0}^M \frac{a_m}{s^{m+1}} (\mathbf{I}_N + \mu \mathbf{L} - s \mathbf{I}_N)^m \mathbf{y} \quad (38)$$

where (a) is a truncated *Taylor Series Expansion* (TSE) of the matrix inverse function of  $M + 1$  terms,  $a_m = (-1)^m$  are the TSE coefficients, and  $s$  is the fixed point at which the approximation is computed. For simplicity, consider the asymmetric random-walk Laplacian  $\mathbf{L}_{rw} \triangleq \mathbf{D}^{-1} \mathbf{L}$  instead of  $\mathbf{L}$  ( $\mathbf{D}$  is a diagonal degree matrix), with real eigenvalues<sup>3</sup>  $\lambda_i \in [0, 2]$ . Thus, fixed point  $s$  can be chosen as the midpoint of the eigenvalue range  $[1, 1 + 2\mu]$  for  $\mathbf{I}_N + \mu \mathbf{L}_{rw}$ , i.e.,  $s = 1 + \mu$ . Setting  $M = 1$  we get

$$\mathbf{x}^* \approx \left( \frac{1}{1 + \mu} \mathbf{I}_N + \frac{-1}{(1 + \mu)^2} (\mu \mathbf{L}_{rw} - \mu \mathbf{I}_N) \right) \mathbf{y} \quad (39)$$

$$= \left( \frac{\mathbf{I}_N + \mu \mathbf{I}_N - \mu \mathbf{L}_{rw} + \mu \mathbf{I}_N}{(1 + \mu)^2} \right) \mathbf{y} \quad (40)$$

$$= (1 + \mu)^{-2} ((1 + 2\mu) \mathbf{I}_N - \mu \mathbf{L}_{rw}) \mathbf{y}. \quad (41)$$

Given that  $\mathbf{L}_{rw}$  is a high-pass filter, (41) states that output  $\mathbf{x}^*$  is a scaled version of  $\mathbf{y}$  filtered by low-pass filter  $(1 + 2\mu) \mathbf{I}_N - \mu \mathbf{L}_{rw}$ .

Suppose now that the underlying graph  $\mathcal{G}$  is a line graph, and hence  $\mathbf{L}_{rw}$  is a tri-diagonal matrix. Then,

$$x_i^* = (1 + \mu)^{-2} [(1 + 2\mu) y_i - \mu(-w_{i-1,i} y_{i-1} + y_i - w_{i,i+1} y_{i+1})] \quad (42)$$

$$= (1 + \mu)^{-2} [(1 + 2\mu) y_i - \mu(w_{i-1,i}(y_i - y_{i-1}) - w_{i,i+1}(y_{i+1} - y_i))] \quad (43)$$

where  $w_{i-1,i} + w_{i,i+1} = 1$  due to normalization in  $\mathbf{L}_{rw}$ . Defining *discrete gradient*  $\nabla y_i \triangleq y_i - y_{i-1}$ , we rewrite  $x_i^*$  as

$$x_i^* = (1 + \mu)^{-2} ((1 + 2\mu) y_i - \mu(w_{i-1,i} \nabla y_i - w_{i,i+1} \nabla y_{i+1})). \quad (44)$$

If this graph filter is applied iteratively (with edge weights recomputed based on updated signal in each iteration), then at iteration  $t$ ,

$$x_i^{t+1} - x_i^t = (1 + \mu)^{-2} [(1 + 2\mu) x_i^t - \mu(w_{i-1,i} \nabla x_i^t - w_{i,i+1} \nabla x_{i+1}^t)] - x_i^t \quad (45)$$

$$= (1 + \mu)^{-2} ((-\mu^2) x_i^t + \mu(w_{i-1,i} \nabla x_i^t - w_{i,i+1} \nabla x_{i+1}^t)) \quad (46)$$

$$\stackrel{(a)}{\approx} \frac{\mu}{(1 + \mu)^2} (w_{i-1,i} \nabla x_i^t - w_{i,i+1} \nabla x_{i+1}^t) \quad (47)$$

where in (a) we ignore the first term scaled by  $\mu^2$ , which is a good approximation when  $\mu$  is small. Recall that edge weight  $w_{i,i+1}$  is defined in a signal-dependent manner:

<sup>3</sup>Random-walk Laplacian  $\mathbf{L}_{rw} = \mathbf{D}^{-1} \mathbf{L}$  is a similarity transform of symmetric normalized Laplacian  $\mathbf{L}_n = \mathbf{D}^{-1/2} \mathbf{L} \mathbf{D}^{-1/2}$  that has real eigenvalues in range  $[0, 2]$  [10].

$$\begin{aligned} w_{i,i+1} &= \exp \left( -\frac{\|\mathbf{f}_i - \mathbf{f}_{i+1}\|_2^2}{\sigma_f^2} - \frac{|x_i - x_{i+1}|}{\sigma_x^2} \right) \\ &= \exp \left( -\frac{\|\mathbf{f}_i - \mathbf{f}_{i+1}\|_2^2}{\sigma_f^2} - \frac{|\nabla x_{i+1}|}{\sigma_x^2} \right) \end{aligned} \quad (48)$$

where  $w_{i,i+1} \rightarrow 0$  when  $|\nabla x_{i+1}| \rightarrow \infty$ . Similarly done in [61], we compare (47) to anisotropic diffusion proposed by Perona and Malik [62]:

$$\frac{\partial x}{\partial t} = c(x) \nabla x \quad (49)$$

where  $c(x)$  is the nonlinear diffusion coefficient, typically defined as

$$c(x) = g(\|\nabla x\|) \quad (50)$$

where  $g(\cdot)$  is an *edge preserving function*, i.e.,  $g(s) \rightarrow 0$  when  $s \rightarrow \infty$ . By interpreting signal-dependent edge weights  $w_{i,i+1}$  as nonlinear diffusion coefficients that is edge preserving (50), we see now that (47) is a variant of anisotropic diffusion similar to (49). Given that Perona and Malik's anisotropic diffusion (*total variation* (TV) [63] is an example) is known to promote PWC signal reconstruction— $\frac{\partial x}{\partial t} = 0$  in (49) if  $\nabla x = 0$  (constant signal) or if  $c(x) = g(\|\nabla x\|) = 0$  (signal discontinuity), iterative GLR with signal-dependent edge weights also promotes PWC signal reconstruction.

## B. GGLR Promoting PWL Signal Reconstruction

Given that iterative GLR with signal-dependent edge weights promotes PWC signal reconstruction, as discussed in Appendix A, applying iterative GLR to horizontal/vertical gradient of a pixel row/column would mean PWC gradient reconstruction. A piecewise linear (PWL) signal has PWC gradient, and thus promotion of PWC gradient reconstruction via GGLR implies promotion of PWL signal reconstruction.

## C. PnP ADMM for Two Auxiliary Variables

Recall that the ADMM objective function when two auxiliary variables  $\mathbf{z}$  and  $\tilde{\mathbf{z}}$  are introduced is

$$\begin{aligned} \min_{\mathbf{x}, \mathbf{z}, \tilde{\mathbf{z}}} & \|\mathbf{y} - \mathbf{Ax}\|_2^2 + \mu \mathbf{z}^\top \mathcal{L} \mathbf{z} + \boldsymbol{\lambda}^\top (\mathbf{x} - \mathbf{z}) + \frac{\rho}{2} \|\mathbf{x} - \mathbf{z}\|_2^2 \\ & + \tilde{\mu} \tilde{\mathbf{z}}^\top \tilde{\mathcal{L}} \tilde{\mathbf{z}} + \tilde{\boldsymbol{\lambda}}^\top (\mathbf{x} - \tilde{\mathbf{z}}) + \frac{\tilde{\rho}}{2} \|\mathbf{x} - \tilde{\mathbf{z}}\|_2^2. \end{aligned} \quad (51)$$

We solve (51) iteratively by solving for variables  $\mathbf{x}$ ,  $\mathbf{z}$  and  $\tilde{\mathbf{z}}$  and updating Lagrange multipliers  $\boldsymbol{\lambda}$  and  $\tilde{\boldsymbol{\lambda}}$  in order as

$$\mathbf{x}^{(k+1)} = \arg \min_{\mathbf{x}} \|\mathbf{y} - \mathbf{Ax}\|_2^2 + \frac{\rho}{2} \|\mathbf{x} - \hat{\mathbf{x}}^{(k)}\|_2^2 \quad (52)$$

$$\mathbf{z}^{(k+1)} = \arg \min_{\mathbf{z}} \mu \mathbf{z}^\top \mathcal{L} \mathbf{z} + \frac{\rho}{2} \|\mathbf{z} - \hat{\mathbf{z}}^{(k)}\|_2^2 \quad (53)$$

$$\tilde{\mathbf{z}}^{(k+1)} = \arg \min_{\tilde{\mathbf{z}}} \tilde{\mu} \tilde{\mathbf{z}}^\top \tilde{\mathcal{L}} \tilde{\mathbf{z}} + \frac{\tilde{\rho}}{2} \|\tilde{\mathbf{z}} - \hat{\tilde{\mathbf{z}}}^{(k)}\|_2^2 \quad (54)$$

$$\hat{\boldsymbol{\lambda}}^{(k+1)} = \hat{\boldsymbol{\lambda}}^{(k)} + (\mathbf{x}^{(k+1)} - \mathbf{z}^{(k+1)}) \quad (55)$$

$$\hat{\tilde{\boldsymbol{\lambda}}}^{(k+1)} = \hat{\tilde{\boldsymbol{\lambda}}}^{(k)} + (\mathbf{x}^{(k+1)} - \tilde{\mathbf{z}}^{(k+1)}) \quad (56)$$

where

$$\hat{\boldsymbol{\lambda}}^{(k)} = (1/\rho)\boldsymbol{\lambda}^{(k)} \quad (57)$$

$$\hat{\mathbf{x}}^{(k)} = \mathbf{z}^{(k)} - \hat{\boldsymbol{\lambda}}^{(k)} + \tilde{\mathbf{z}}^{(k)} - \hat{\tilde{\boldsymbol{\lambda}}}^{(k)} \quad (58)$$

$$\hat{\tilde{\boldsymbol{\lambda}}}^{(k)} = (1/\rho)\tilde{\boldsymbol{\lambda}}^{(k)} \quad (59)$$

$$\hat{\mathbf{z}}^{(k)} = \mathbf{x}^{(k+1)} + \hat{\boldsymbol{\lambda}}^{(k)} \quad (60)$$

$$\hat{\tilde{\mathbf{z}}}^{(k)} = \mathbf{x}^{(k+1)} + \hat{\tilde{\boldsymbol{\lambda}}}^{(k)}. \quad (61)$$

(52), (53) and (54) are convex quadratic equations whose respective solutions  $\mathbf{x}^{(k+1)}$ ,  $\mathbf{z}^{(k+1)}$  and  $\tilde{\mathbf{z}}^{(k+1)}$  can be obtained by solving linear systems:

$$(2\mathbf{A}^\top \mathbf{A} + \rho \mathbf{I}_N) \mathbf{x}^{(k+1)} = 2\mathbf{A}^\top \mathbf{y} + \rho \hat{\mathbf{x}}^{(k)} \quad (62)$$

$$(\mathbf{I}_N + \frac{2\mu}{\rho} \mathcal{L}) \mathbf{z}^{(k+1)} = \hat{\mathbf{z}}^{(k)} \quad (63)$$

$$(\mathbf{I}_N + \frac{2\tilde{\mu}}{\tilde{\rho}} \tilde{\mathcal{L}}) \tilde{\mathbf{z}}^{(k+1)} = \hat{\tilde{\mathbf{z}}}^{(k)}. \quad (64)$$

These linear systems can be solved using *conjugate gradient* (CG) [49] efficiently without matrix inverse, as described in Section IV-B2.

## REFERENCES

- [1] Michael Elad and Michal Aharon, "Image denoising via sparse and redundant representations over learned dictionaries," *IEEE Transactions on Image processing*, vol. 15, no. 12, pp. 3736–3745, 2006.
- [2] Amir Beck and Marc Teboulle, "Fast gradient-based algorithms for constrained total variation image denoising and deblurring problems," *IEEE transactions on image processing*, vol. 18, no. 11, pp. 2419–2434, 2009.
- [3] Shuhang Gu, Lei Zhang, Wangmeng Zuo, and Xiangchu Feng, "Weighted nuclear norm minimization with application to image denoising," *2014 IEEE Conference on Computer Vision and Pattern Recognition*, pp. 2862–2869, 2014.
- [4] Lei Zhang and Wangmeng Zuo, "Image restoration: From sparse and low-rank priors to deep priors [lecture notes]," *IEEE Signal Processing Magazine*, vol. 34, no. 5, pp. 172–179, 2017.
- [5] Siavash Arjomand Bigdeli, Matthias Zwicker, Paolo Favaro, and Meiguang Jin, "Deep mean-shift priors for image restoration," *Advances in Neural Information Processing Systems*, vol. 30, 2017.
- [6] Xingchao Peng, Judy Hoffman, X Yu Stella, and Kate Saenko, "Fine-to-coarse knowledge transfer for low-res image classification," in *IEEE International Conference on Image Processing (ICIP)*, 2016.
- [7] Hugo Touvron, Andrea Vedaldi, Matthijs Douze, and Hervé Jégou, "Fixing the train-test resolution discrepancy," *Advances in neural information processing systems*, vol. 32, 2019.
- [8] Vishal Monga, Yuelong Li, and Yonina C. Eldar, "Algorithm unrolling: Interpretable, efficient deep learning for signal and image processing," *IEEE Signal Processing Magazine*, vol. 38, no. 2, pp. 18–44, 2021.
- [9] Yaodong Yu, Sam Buchanan, Druv Pai, Tianzhe Chu, Ziyang Wu, Shengbang Tong, Benjamin D. Haeffele, and Y. Ma, "White-box transformers via sparse rate reduction," *ArXiv*, vol. abs/2306.01129, 2023.
- [10] Antonio Ortega, Pascal Frossard, Jelena Kovacevic, Jose M. F. Moura, and Pierre Vandergheynst, "Graph signal processing: Overview, challenges, and applications," *Proceedings of the IEEE*, vol. 106, no. 5, pp. 808–828, 2018.
- [11] G. Cheung, E. Magli, Y. Tanaka, and M. Ng, "Graph spectral image processing," in *Proceedings of the IEEE*, May 2018, vol. 106, no. 5, pp. 907–930.
- [12] J. Pang and G. Cheung, "Graph Laplacian regularization for inverse imaging: Analysis in the continuous domain," in *IEEE Transactions on Image Processing*, April 2017, vol. 26, no. 4, pp. 1770–1785.
- [13] X. Liu, G. Cheung, X. Wu, and D. Zhao, "Random walk graph Laplacian based smoothness prior for soft decoding of JPEG images," *IEEE Transactions on Image Processing*, vol. 26, no. 2, pp. 509–524, February 2017.
- [14] X. Liu, G. Cheung, X. Ji, D. Zhao, and W. Gao, "Graph-based joint dequantization and contrast enhancement of poorly lit JPEG images," *IEEE Transactions on Image Processing*, vol. 28, no. 3, pp. 1205–1219, March 2019.
- [15] Y. Bai, G. Cheung, X. Liu, and W. Gao, "Graph-based blind image deblurring from a single photograph," *IEEE Transactions on Image Processing*, vol. 28, no. 3, pp. 1404–1418, 2019.
- [16] Chinthaka Dinesh, Gene Cheung, and Ivan V. Bajic, "Point cloud denoising via feature graph laplacian regularization," *IEEE Transactions on Image Processing*, vol. 29, pp. 4143–4158, 2020.
- [17] Jin Zeng, Gene Cheung, Michael Ng, Jiahao Pang, and Cheng Yang, "3d point cloud denoising using graph laplacian regularization of a low dimensional manifold model," *IEEE Transactions on Image Processing*, vol. 29, pp. 3474–3489, 2020.
- [18] Fei Chen, Gene Cheung, and Xue Zhang, "Fast & robust image interpolation using gradient graph Laplacian regularizer," in *IEEE International Conference on Image Processing (ICIP)*, 2021.
- [19] Chinthaka Dinesh, Gene Cheung, and Ivan V. Bajic, "Point cloud video super-resolution via partial point coupling and graph smoothness," *IEEE Transactions on Image Processing*, vol. 31, pp. 4117–4132, 2022.
- [20] Fei Chen, Gene Cheung, and Xue Zhang, "Manifold graph signal restoration using gradient graph Laplacian regularizer," *IEEE Transactions on Signal Processing*, vol. 72, pp. 744–761, 2024.
- [21] O. Axelsson and G. Linskog, "On the rate of convergence of the preconditioned conjugate gradient method," *Numerische Mathematik*, vol. 48, no. 5, pp. 499–523, 1986.
- [22] Stanley H. Chan, "Performance analysis of plug-and-play ADMM: A graph signal processing perspective," *IEEE Transactions on Computational Imaging*, vol. 5, pp. 274–286, 2018.
- [23] Dzmitry Bahdanau, Kyunghyun Cho, and Yoshua Bengio, "Neural machine translation by jointly learning to align and translate," *CoRR*, vol. abs/1409.0473, 2014.
- [24] Ashish Vaswani, Noam Shazeer, Niki Parmar, Jakob Uszkoreit, Llion Jones, Aidan N Gomez, Łukasz Kaiser, and Illia Polosukhin, "Attention is all you need," *Advances in neural information processing systems*, vol. 30, 2017.
- [25] Syed Waqas Zamir, Aditya Arora, Salman Hameed Khan, Munawar Hayat, Fahad Shahbaz Khan, and Ming-Hsuan Yang, "Restormer: Efficient transformer for high-resolution image restoration," *CVPR*, pp. 5718–5729, 2022.
- [26] Kai Zhang, Wangmeng Zuo, Yunjin Chen, Deyu Meng, and Lei Zhang, "Beyond a Gaussian denoiser: Residual learning of deep CNN for image denoising," *IEEE transactions on image processing*, vol. 26, no. 7, pp. 3142–3155, 2017.
- [27] Kai Zhang, Wangmeng Zuo, and Lei Zhang, "FFDNet: Toward a fast and flexible solution for CNN-based image denoising," *IEEE Transactions on Image Processing*, vol. 27, no. 9, pp. 4608–4622, 2018.
- [28] Shi Guo, Zifei Yan, Kai Zhang, Wangmeng Zuo, and Lei Zhang, "Toward convolutional blind denoising of real photographs," in *IEEE/CVF conference on computer vision and pattern recognition*, 2019.
- [29] Raviteja Vemulapalli, Oncel Tuzel, and Ming-Yu Liu, "Deep gaussian conditional random field network: A model-based deep network for discriminative denoising," in *IEEE conference on computer vision and pattern recognition*, 2016.
- [30] Jingyun Liang, Jie Cao, Guolei Sun, K. Zhang, Luc Van Gool, and Radu Timofte, "Swinir: Image restoration using swin transformer," *IEEE International Conference on Computer Vision Workshops (ICCVW)*, pp. 1833–1844, 2021.
- [31] Zhendong Wang, Xiaodong Cun, Jianmin Bao, Wengang Zhou, Jianzhuang Liu, and Houqiang Li, "Uformer: A general u-shaped transformer for image restoration," in *Proceedings of the IEEE/CVF conference on computer vision and pattern recognition*, 2022, pp. 17683–17693.
- [32] Syed Waqas Zamir, Aditya Arora, Salman Khan, Munawar Hayat, Fahad Shahbaz Khan, Ming-Hsuan Yang, and Ling Shao, "Multi-stage progressive image restoration," in *Proceedings of the IEEE/CVF conference on computer vision and pattern recognition*, 2021, pp. 14821–14831.
- [33] Haoyu Chen, Jinjin Gu, Yihao Liu, Salma Abdel Magid, Chao Dong, Qiong Wang, Hanspeter Pfister, and Lei Zhu, "Masked image training for generalizable deep image denoising," *IEEE Conference on Computer Vision and Pattern Recognition (CVPR)*, pp. 1692–1703, 2023.
- [34] Rino Yoshida, Kazuya Kodama, Huy Vu, Gene Cheung, and Takayuki Hamamoto, "Unrolling graph total variation for light field image denoising," *IEEE International Conference on Image Processing (ICIP)*, 2022.

[35] Carlo Tomasi and Roberto Manduchi, "Bilateral filtering for gray and color images," in *IEEE International Conference on Computer Vision*, 1998.

[36] A. Buades, B. Coll, and J.-M. Morel, "A non-local algorithm for image denoising," in *IEEE Computer Society Conference on Computer Vision and Pattern Recognition*, 2005, vol. 2, pp. 60–65.

[37] Kostadin Dabov, Alessandro Foi, Vladimir Katkovnik, and Karen Egiazarian, "Image denoising by sparse 3-d transform-domain collaborative filtering," *IEEE Transactions on image processing*, vol. 16, no. 8, pp. 2080–2095, 2007.

[38] Jun Xu, Lei Zhang, and David Zhang, "A trilateral weighted sparse coding scheme for real-world image denoising," in *Proceedings of the European Conference on Computer Vision (ECCV)*, September 2018.

[39] Yingkun Hou, Jun Xu, Mingxia Liu, Guanghai Liu, Li Liu, Fan Zhu, and Ling Shao, "Nlh: A blind pixel-level non-local method for real-world image denoising," *IEEE Transactions on Image Processing*, vol. 29, pp. 5121–5135, 2020.

[40] Jin Zeng, Jiahao Pang, Wenxiu Sun, and Gene Cheung, "Deep graph Laplacian regularization for robust denoising of real images," in *IEEE/CVF Conference on Computer Vision and Pattern Recognition Workshops*, 2019.

[41] Huy Vu, Gene Cheung, and Yonina C Eldar, "Unrolling of deep graph total variation for image denoising," in *IEEE International Conference on Acoustics, Speech and Signal Processing (ICASSP)*, 2021.

[42] Matthieu Terris, Thomas Moreau, Nelly Pustelnik, and Julian Tachella, "Equivariant plug-and-play image reconstruction," in *2024 IEEE/CVF Conference on Computer Vision and Pattern Recognition (CVPR)*, 2024, pp. 25255–25264.

[43] Marien Renaud, Jean Prost, Arthur Leclaire, and Nicolas Papadakis, "Plug-and-play image restoration with stochastic denoising regularization," in *Proceedings of the 41st International Conference on Machine Learning*. 2024, ICML'24, JMLR.org.

[44] Andrea Ebner and Markus Haltmeier, "Plug-and-play image reconstruction is a convergent regularization method," *IEEE Transactions on Image Processing*, vol. 33, pp. 1476–1486, 2024.

[45] Kartheek Kumar Reddy Nareddy, Abijith Jagannath Kamath, and Chandra Sekhar Seelamantula, "Image restoration with generalized l2 loss and convergent plug-and-play priors," in *ICASSP 2024 - 2024 IEEE International Conference on Acoustics, Speech and Signal Processing (ICASSP)*, 2024, pp. 2515–2519.

[46] Karol Gregor and Yann LeCun, "Learning fast approximations of sparse coding," in *Proceedings of the 27th International Conference on International Conference on Machine Learning*, Madison, WI, USA, 2010, ICML'10, p. 399–406, Omnipress.

[47] John R. Hershey, Jonathan Le Roux, and Felix Weninger, "Deep unfolding: Model-based inspiration of novel deep architectures," *ArXiv*, vol. abs/1409.2574, 2014.

[48] Yan Yang, Jian Sun, Huibin Li, and Zongben Xu, "Admm-csnet: A deep learning approach for image compressive sensing," *IEEE Transactions on Pattern Analysis and Machine Intelligence*, vol. 42, pp. 521–538, 2020.

[49] Magnus R. Hestenes and Eduard Stiefel, "Methods of conjugate gradients for solving linear systems," *Journal of research of the National Bureau of Standards*, vol. 49, pp. 409–435, 1952.

[50] Zhou Wang, Alan C Bovik, Hamid R Sheikh, and Eero P Simoncelli, "Image quality assessment: from error visibility to structural similarity," *IEEE transactions on image processing*, vol. 13, no. 4, pp. 600–612, 2004.

[51] Stefan Roth and Michael J Black, "Fields of experts," *International Journal of Computer Vision*, vol. 82, pp. 205–229, 2009.

[52] Kai Zhang, Wangmeng Zuo, Shuhang Gu, and Lei Zhang, "Learning deep CNN denoiser prior for image restoration," in *Proceedings of the IEEE conference on computer vision and pattern recognition*, 2017, pp. 3929–3938.

[53] Kai Zhang, Yawei Li, Wangmeng Zuo, Lei Zhang, Luc Van Gool, and Radu Timofte, "Plug-and-play image restoration with deep denoiser prior," *IEEE Transactions on Pattern Analysis and Machine Intelligence*, vol. 44, no. 10, pp. 6360–6376, 2022.

[54] Josue Anaya and J Barbu, "Renoir-a dataset for real low-light noise image reduction," *J Visual Commun Image Represent*, 2014.

[55] Seonghyeon Nam, Youngbae Hwang, Yasuyuki Matsushita, and Seon Joo Kim, "A holistic approach to cross-channel image noise modeling and its application to image denoising," in *Proceedings of the IEEE conference on computer vision and pattern recognition*, 2016, pp. 1683–1691.

[56] Radu Timofte, Vincent De Smet, and Luc Van Gool, "A+: Adjusted anchored neighborhood regression for fast super-resolution," in *Computer Vision–ACCV 2014: 12th Asian Conference on Computer Vision, Singapore, Singapore, November 1–5, 2014, Revised Selected Papers, Part IV 12*. Springer, 2015, pp. 111–126.

[57] Daniel Zoran and Yair Weiss, "From learning models of natural image patches to whole image restoration," in *2011 international conference on computer vision*. IEEE, 2011, pp. 479–486.

[58] Anat Levin, Yair Weiss, Fredo Durand, and William T Freeman, "Understanding and evaluating blind deconvolution algorithms," in *2009 IEEE conference on computer vision and pattern recognition*. IEEE, 2009, pp. 1964–1971.

[59] Jakob Kruse, Carsten Rother, and Uwe Schmidt, "Learning to push the limits of efficient FFT-based image deconvolution," in *Proceedings of the IEEE International Conference on Computer Vision*, 2017, pp. 4586–4594.

[60] Yuanchao Bai, Gene Cheung, Xianming Liu, and Wen Gao, "Blind image deblurring via reweighted graph total variation," in *2018 IEEE International Conference on Acoustics, Speech and Signal Processing (ICASSP)*. IEEE, 2018, pp. 1822–1826.

[61] D. Barash, "Fundamental relationship between bilateral filtering, adaptive smoothing, and the nonlinear diffusion equation," *IEEE Transactions on Pattern Analysis and Machine Intelligence*, vol. 24, no. 6, pp. 844–847, 2002.

[62] P. Perona and J. Malik, "Scale-space and edge detection using anisotropic diffusion," *IEEE Transactions on Pattern Analysis and Machine Intelligence*, vol. 12, no. 7, pp. 629–639, 1990.

[63] A. Chambolle and P.-L. Lions, "Image recovery via total variation minimization and related problems," *Numerische Mathematik*, vol. 76, no. 2, pp. 167–188, 1997.